Coarse-grid simulation of reacting and non-reacting gas-particle flows

Annual Technical Progress Report

September 14, 2002 – September 13, 2003

Author: Sankaran Sundaresan

Department of Chemical Engineering

Princeton University

Princeton, NJ 08544

(609) 258-4583 (tel)

(609) 258-0211 (fax)

sundar@princeton.edu

March 2004

Award # DE-FC26-00NT409071

DOE Vision 21 Virtual Demonstration Initiative

Name of the submitting organization: Princeton University, Princeton, NJ 08544

Disclaimer

Abstract

The principal goal of this project, funded under the *DOE Vision 21 Virtual Demonstration Initiative* is virtual demonstration of circulating fluidized bed performance. We had proposed a *virtual demonstration tool*, which is based on the open-domain CFD code MFIX. The principal challenge funded through this grant is to devise and implement in this CFD code sound physical models for the rheological characteristics of the gas-particle mixtures. Within the past year, which was the third year of the project, we have made the following specific advances.

(a) We have completed a study of the impact of sub-grid models of different levels of detail on the results obtained in coarse-grid simulations of gas-particle flow.

(b) We have also completed a study of a model problem to understand the effect of wall friction, which was proved in our earlier work to be very important for stable operation of standpipes in a circulating fluidized bed circuit.

These are described in a greater detail in this report.

Table of Contents

1. Introduction[1]

The principal goal of our project, funded under the *DOE Vision 21 Virtual Demonstration Initiative* is virtual demonstration of circulating fluidized bed (CFB) performance. Virtual demonstration of CFB performance requires modeling and simulation of the entire spectrum of gas-particle flow conditions ranging from dense phase flows in standpipes to dilute phase flow conditions of risers.

We had proposed a *virtual demonstration tool*, which is based on the open-domain CFD code MFIX, originally developed at NETL. MFIX is based on a model framework in which the gas and particle phases are treated as interpenetrating continua. The general structure of Eulerian equations of motion for each of the phases is well understood, although specific constitutive equations describing the rheological behavior of gas-particle suspensions are still being developed. MFIX includes the capability to carry out reactive flow simulations, so the tool that we have set out to develop will permit both cold flow and reactive flow simulations. The principal challenge funded through this grant is to devise and implement in MFIX sound physical models for the rheological characteristics of the gas-particle mixtures.

2. Specific Objectives of Proposed Research

The volume fraction of particles in dense fluidized beds, standpipes and valves is usually sufficiently large that the particles make enduring contact with multiple neighbors. In such instances, stress transmission between particles, and between particles and bounding solid surfaces occurs predominantly through frictional interactions. In this regime of flow, when the strength of frictional interaction between particles becomes sufficiently weak, flow of gas-solid suspension becomes unstable and a bubbly suspension results. Once formed, these bubbles dictate the macroscale flow characteristics, and therefore detailed CFD simulation of suspensions in this regime should account for the dynamics associated with the gas bubbles. This is possible only if frictional stresses are modeled properly. We have developed and implemented a model for frictional rheology into MFIX and thus, we have a framework for realistic representation of

[1] The first three sections are repeated from last year's Technical Progress Report. It is merely intended to provide an overview of the overall project and the objectives.

frictional stresses. One of the objectives of our research is to develop methodologies for evaluating frictional model parameters experimentally.

Another objective of our research is to develop methodologies for practical simulation of gas-particle flows in fast-fluidized beds and risers, where the particle concentration is typically in the range of 1-30 vol %. In our past research, we have shown that meso-scale structures that take the form of clusters and streamers, which have been observed in risers, can be captured qualitatively through transient integration of continuum equations for the gas and particle phases. These structures arise as a result of two instability mechanisms, both of which are accounted for in a rheological model deduced in the literature by adapting the kinetic theory of gases to gas-particle mixtures. These meso-scale structures are too small in size to be resolved in simulations of flow in large process vessels, and are invariably invisible in the coarse-grid simulations. Yet, they affect the flow characteristics profoundly; in particular, they alter the effective interaction force that couples the gas and particle phases, and dramatically increase the effective viscosities of the two phases. We had proposed to develop a more practical approach, where we simulate the dynamics of only the large clusters using coarse grids and account for the effects of smaller, unresolved clusters through suitable sub-grid approximations. Specifically, we had proposed to develop such sub-grid models and implement them into our *virtual demonstration tool*.

3. Specific Goals and Tasks Proposed

In order to achieve these objectives, we had proposed a three year long research program involving a combination of simple laboratory experiments on frictional stress in dense gas-particle systems and computational experiments on statistical characteristics of mesoscale structures. The goals and tasks for each of the three years, as outlined in our original proposal, are shown in Tables 1-3.

4. **Progress at the End of Year 3**

We have pursued the goals listed in Table 3, by undertaking the tasks listed there. However, we could not complete all the tasks because of problems with our computer cluster. Consequently, we requested a one-year, no-cost extension of the grant (extending the contract for a fourth year), which was approved by the Department of Energy. The specific accomplishments in the third year of the project are as follows:

Further Computational Experiments on Mesoscale Structures

Our early studies on meso-scale structures can be found in Agrawal et al. (2001) and the technical progress reports for the years 2001 and 2002. We have continued our studies on meso-scale structures in gas-particle flows, where we have now focused on the behavior of various time- and space- smoothed quantities to fully understand how each of them contributes to effective sub-grid closures. A manuscript based on this analysis is under preparation. Briefly, we have demonstrated through a detailed analysis of the fluctuating part of the local pressure gradient that the correct way to account for the influence of sub-grid microstructure on the effective drag force is indeed through a stochastic drag force term (as mentioned in 2002 Technical Progress Report). The stochastic part of the interphase drag arises from the random nature of the formation and breakup of meso-scale clusters. Specific details of this stochastic sub-grid model can be found in the attached manuscript by Andrews et al. (2004). Our simulations found little evidence for an effective added mass force term proposed by Zhang & VanderHeyden (2002). We have also constructed a stochastic sub-grid model for the effective stresses.

Additional Coarse-grid simulations

We have performed many 2-D coarse-grid simulations of gas-particle flow in a vertical channel to assess the impact of the sub-grid models and the sensitivity of the results to various components of the sub-grid models. A detailed manuscript outlining this work, Andrews, et al. (2004), is attached. The main findings of this work are summarized below.

Our study clearly showed that the results obtained in coarse-grid integration of the microscopic equations for gas-particle flows in large process vessels can change appreciably if sub-grid corrections to account for the effects of unresolved structures are included. The most dramatic difference occurred in our simulations when a simple *time-averaged* sub-grid model was added to the *no sub-grid* model case. Although the level of sophistication of the sub-grid model did make a difference in the quantitative results in our simulations, even a simple time-averaged sub-grid model appeared to capture the main qualitative effects.

The simple time-averaged sub-grid model is, in a strict sense, flawed, as there is no separation of time scales between the unresolved (sub-grid) structures and those resolved in the coarse-grid simulations. To account for this lack of separation of time scale, an enhancement of the time-averaged sub-grid model that took the form of a stochastic correction to the drag coefficient was implemented. It was found that such a stochastic sub-grid model yielded qualitatively the same results as the time-averaged sub-grid model. Thus the lack of separation of time scales does not appear to be a severe deficiency.

We have also examined the effect of stochastic fluctuations at the riser inlet on the flow structure produced in the riser, and demonstrated that the inlet fluctuations aid the development of time-dependent flow structures in the riser, and eliminates spurious solutions which can be predicted by simulations under some conditions.

Working together with DOE scientists (Sreekanth Pannala and Thomas O'Brien) we have also performed several 3-D simulations of flow patterns in a square riser. These simulations (Pannala et al., 2003) were performed to compare predictions with flow structures measured experimentally by Grace and coworkers. These experiments were performed with large and heavy particles (compared to the typical FCC particles) and in a riser with a small cross sectional area. Our scaling estimates suggested that for this specific comparison, sub-grid models would only amount to a small correction, and this was indeed found to be the case.

The studies on riser hydrodynamics that we are currently pursuing are aimed at:

a) An improved understanding of the role of stochastic fluctuations in sub-grid normal stresses and viscosity on the resolved solution structure, and
b) Better articulation of the differences between 2 – D and 3 – D simulations for FCC particles, where we do know from 2 – D simulations that sub-grid corrections are important.

Experiments in friction-dominated flow regime

We had demonstrated in our earlier work that wall friction and granular contact stresses play important roles in stable operation of standpipes (Srivastava et al., 1998; Srivastava & Sundaresan, 2002), and are also important in understanding bed expansion characteristics of fluidized beds (Loezos et al., 2002). We had also constructed a multi-dimensional frictional stress model, implemented it in MFIX and applied it to model flow problems (Srivastava & Sundaresan, 2003). We felt that it is very important to understand the manner in which stick-slip flow occurs in dense granular flow through pipes, in order to develop a better physical understanding of the flow patterns in such a flow regime. To this end, we devised a simple experiment, where we studied the manner in which particles discharged from a tube equipped with a central orifice at the bottom. The details of this study are summarized in the manuscript attached (Muite et al., 2003). This study provides new insight on vibration of the structure associated with stick-slip flow, and an accompanying phenomenon known as silo music. It also shows that the frictional stress models which are currently available are quite primitive.

Standpipe flow

A few years ago, we performed experiments where we examined the CFB performance characteristics at different levels of aeration, probing specifically the flow behavior in the standpipe and the conditions at which the loop instability sets in (Srivastava et al., 1998). It was clear from that study that contact stresses in the particle phase and wall friction played important roles in imparting stability to CFB hydrodynamics. We undertook a study to establish this point in a quantitative sense. We performed simple fluidization and defluidization experiments in tubes of various diameters to extract information on the compressive yield strength of particle assemblies at various volume fractions and wall friction parameters. We used this information to show that the standpipe performance data could be explained quantitatively on the basis of wall friction and granular stresses (Srivastava & Sundaresan, 2002).

Having ascertained that granular stresses and wall friction played important roles in standpipe flows, we set out to understand the general characteristics of these quantities for a

variety of particles. This study (Loezos et al., 2002), demonstrated the robustness of the dependence of granular stress on particle volume fraction (for seven different types of particles) and the consistent role of wall friction. Therefore a generic model for dense phase flow of Geldart type A powders in devices such as standpipes should be possible.

We assembled a simple one-dimensional model for the performance characteristics of a standpipe equipped with aeration taps and with a slide valve at the bottom, and are currently exploring the range of performances afforded by this system. This work will be completed in the months ahead.

5. Activities Planned for the remainder of the contract

As a natural continuation of our research, we will address the following tasks in the remaining duration of the contract.

Riser flow problems

a) improve our understanding of the role of stochastic fluctuations in sub-grid normal stresses and viscosity on the resolved structure,
b) undertake additional 3 – D simulations to better understand the differences between 2 – D and 3 – D.

Standpipe flow modeling

c) complete analysis of a one-dimensional model for aerated standpipes equipped with a slide valve,

In addition, we will also complete the specific tasks summarized in our original proposal (see Table 3).

6. Deliverables We Had Proposed[2]

The deliverables in this project include advanced process models and a virtual demonstration tool. The work proposed will significantly advance the knowledge base in the field of gas-solid flow, which is critical element in DOE's Vision 21. The specific deliverables that we had anticipated from our research are as follows:

a) Mathematical model for frictional stresses in dense suspensions, which is supported by experimental data on a variety of powders.
b) Simple experimental protocol to determine the parameters appearing in this frictional model, and methodology to determine these parameters from experimental data.
c) A version of MFIX code, with this frictional model implemented and validated.
d) A fundamentally based sub-grid model for effective drag force, stresses and dispersion, which is deduced through scores of computational experiments and theoretical analysis, and can be used in coarse-grid simulation of reacting and non-reacting gas-solid flows.
e) A version of MFIX code with the above sub-grid model implemented and validated - which can be used for coarse grid simulation of fluidized bed, spouted bed and circulating fluidized bed reactors, used for gasification, desulfurization and combustion of coal and a variety of other purposes in chemical process industries.

[2] This section is repeated from last year's Technical Progress Report. It is merely intended to provide an overview of the proposed deliverables, which has not changed during the course of the project.

7. Status on Deliverables

It was ascertained in year 1 that for a wide range of particles (materials) which are commonly encountered in CFB applications a simple mathematical model suffices for frictional stresses in dense suspensions (item a in section 5).

We have also developed (in year 1) a simple experimental method for determining the parameters appearing in this frictional model (item b in section 5). This works rather well for particles normally encountered in CFB applications. In year 2, we have examined finer particles to see to what extent the approach can be applied to fine particles. This exercise suggests that, as long as the cohesion between particles is only mild, the approach will work.

We have supplied NETL at the end of year 1 with a version of the MFIX code containing the frictional model (item c in section 5). It is now available for anyone to use. Our computational experiments suggest that this code works satisfactorily in applications where there are no stagnant domains.

We now have sub-grid models for drag and stresses (Andrews et al., 2004), and dispersion (Loezos & Sundaresan, 2002), which should be applied in coarse-grid simulation of non-reacting flows (item d in section 5). All of these have been implemented in MFIX, delivered to NETL, and are now available in MFIX for general use. We have also delivered to NETL our stochastic model for inlet fluctuations (and associated computer code, that is readily inserted into MFIX).

8. Bibliography

K. Agrawal, P. N. Loezos, M. Syamlal and S. Sundaresan, "The Role of Meso-scale Structures in Rapid Gas-solid Flows", *J. Fluid Mech.*, **445**, 151 – 185 (2001).

A. T. Andrews, P. N. Loezos and S. Sundaresan, "Coarse-grid Simulation of Gas-Particle Flows in Vertical Risers", paper presented at 2003 AIChE Annual Meeting and submitted to Journal of Fluid Mechanics (2004).

P. N. Loezos & S. Sundaresan, "Simulation of dispersion in gas-particle flows through a riser", *Circulating Fluidized Beds* **7** (2002).

P. N. Loezos, P. Costamagna & S. Sundaresan, "The role of contact stresses and wall friction on fluidization", *Chem. Eng. Sci.*, **57**, 5123 – 5141 (2002).

B. Muite, S. F. Quinn, S. Sundaresan and K. K. Rao, "Silo Music and Silo Quake: Granular Flow Induced Vibration", paper presented at 2003 AIChE Annual Meeting and submitted to Powder Technology (2003).

S. Pannala, T. O'Brien, A. Andrews & S. Sundaresan, "Gas-particle flow in a square riser", paper presented at the AIChE Annual Meeting, San Francisco, November 2003.

A. Srivastava, K. Agrawal, S. Sundaresan, S. B. Reddy Karri and T. M. Knowlton, "Dynamics of gas-particle flow in circulating fluidized beds", *Powder Technology*, **100**, 173 – 182 (1998).

A. Srivastava & S. Sundaresan, "Role of wall friction in fluidization and standpipe flow", *Powder Technology* **124**, 45 – 54 (2002).

A. Srivastava & S. Sundaresan, "Analysis of a Frictional-kinetic model for Gas-Particle Flows", Powder Tech., **129**, 72 – 85 (2003).

D. Z. Zhang and W. B. VanderHeyden, "The effects of mesoscale structures on the macroscopic momentum equations for two-phase flows", *Int. J. Multiphase Flow*, **28**, 805 – 822 (2002).

9. Publications Resulting from This Study

K. Agrawal, P. N. Loezos, M. Syamlal and S. Sundaresan, "The Role of Meso-scale Structures in Rapid Gas-solid Flows", *J. Fluid Mech.*, **445**, 151 – 185 (2001).

M. Al-Adel, D. A. Saville & S. Sundaresan, "The effect of static electrification on gas-solid flows in vertical risers", to appear in *Industrial & Engineering Chemistry Research* (2002).

A. T. Andrews, P. N. Loezos and S. Sundaresan, "Coarse-grid Simulation of Gas-Particle Flows in Vertical Risers", paper presented at 2003 AIChE Annual Meeting and submitted to Journal of Fluid Mechanics (2004).

P. N. Loezos & S. Sundaresan, "Simulation of dispersion in gas-particle flows through a riser", *Circulating Fluidized Beds* **7** (2002).

P. N. Loezos, P. Costamagna & S. Sundaresan, "The role of contact stresses and wall friction on fluidization", *Chem. Eng. Sci.*, **57**, 5123 – 5141 (2002).

B. Muite, S. F. Quinn, S. Sundaresan and K. K. Rao, "Silo Music and Silo Quake: Granular Flow Induced Vibration", paper presented at 2003 AIChE Annual Meeting and submitted to Powder Technology (2003).

A. Srivastava & S. Sundaresan, "Role of wall friction in fluidization and standpipe flow", *Powder Technology* **124**, 45 – 54 (2002).

A. Srivastava & S. Sundaresan, "Analysis of a Frictional-kinetic model for Gas-Particle Flows", Powder Tech., **129**, 72 – 85 (2003).

10. Abbreviations Used in This Report

CFB	–	**C**irculating **F**luidized **B**ed
CFD	–	**C**omputational **F**luid **D**ynamics
DOE	–	**D**epartment **O**f **E**nergy
MFIX	–	**M**ultiphase **F**low with **I**nterphase exchange
NETL	–	**N**ational **E**nergy **T**echnology **L**aboratory
2 – D		two-dimensional
3 – D		three-dimensional

Table 1: Goals and Tasks (Year 1)

Goals

1.1) Establish quantitative estimates for the effects of mesoscale structures on effective drag, stresses and dispersion. (Note: In what follows, unless specifically mentioned otherwise, the analysis will focus on system of uniformly sized particles.)

1.2) Establish if sub-grid models based on the mean characteristics of the mesoscale structures are sufficient for coarse-grid simulations.

1.3) Establish the features of a general frictional stress model for powders

Tasks

1.1) Perform 3-D simulations of gas - particle flows in periodic domains under shear for various particle volume fractions and shear rates, in order to probe the meso-scale structures and their consequences.

- Gather quantitative data on domain-averaged drag, stresses, etc., probing the influence of key dimensionless groups on domain-average quantities and characteristics of meso-scale structures
- Extract qualitative information on shapes of meso-scale structures through inspection of the animation, particularly on how shear and holdup level affect them.
- Develop a fundamentally based sub-grid model.

1.2) 3-D coarse-grid simulations in a large periodic domain (say 50 cm x 50cm x 5m) and different particle volume fractions, in order to probe the necessary features of sub-grid models

- Choose two different grid sizes (say, 2 cm x 2 cm x10 cm and 1 cm x 1cm x 5 cm). For each grid size, devise sub-grid models for time-averaged effective drag, stresses, etc., through highly resolved numerical computations in doubly periodic domain.
- Using these two different grid sizes and the corresponding sub-grid models, perform coarse grid simulations. Compare the domain-averaged results to establish if sub-grid models based on averages of fluctuating quantities are adequate. Identify additional features of sub-grid models that may be needed to render the domain-averaged results nearly grid-size independent.

1.3) Perform fluidization-defluidization experiments on a series of powders and analyze the data in the spirit of the frictional stress mode, refining the model as necessary.

Table 2: Goals and Tasks (Year 2)

Goals

2.1) Assess the adequacy of coarse-grid simulation of gas-particle flow with embedded sub-grid models in the presence of side walls.

2.2) Develop sub-grid models for cylindrical geometry, implement them into the coarse-grid simulator and validate the model/code.

2.3) Bring forth the effect of particle size distribution on meso-scale characteristics.

2.4) Validate frictional stress model

Tasks

2.1) Perform coarse grid simulations in a segment of a vertical channel (50 cm x 50 cm x 5m, as in task **1.2** above) using periodic boundary conditions in the vertical and one of the lateral directions, and grid-size dependent sub-grid models (as in task **1.2** above). Examine the impact of changes in the wall boundary conditions on predicted time-averaged flow behavior. Identify additional features of sub-grid models (such as wall correction) that may be needed to render the domain-averaged results nearly grid-size independent.

2.2) Based on physical understanding of meso-scale structures, acquired during the first year, construct plausible sub-grid models for grids in cylindrical geometry. Carry out 3-D coarse grid-simulations of fully developed flow in a vertical pipe (using periodic boundary conditions in vertical direction) to evaluate the effects of such sub-grid models. Compare coarse-grid simulation results with experimental data.

2.3) Examine the effect of particle size distribution on meso-scale structures by carrying out simulations of the type described in task **1.1** for bimodal particle size distribution.

2.4) Perform bin discharge experiments, simulate this flow problem, and compare model predictions of discharge rates with experimental data.

Table 3: Goals and Tasks (Year 3)

Goals

3.1) Perform 3-D coarse-grid simulations of developing flow in risers and explore entrance and exit effects.
3.2) Implement fundamentally based sub-grid models for mass and heat dispersion induced by the meso-scale structures.
3.3) Demonstrate capability to perform coarse-grid simulation of reacting flow in risers
3.4) Demonstrate capability to carry out simulation of a complete CFB loop

Tasks

3.1) Perform 3-D coarse-grid simulation of gas-particle flows in vertical risers for various combinations of gas and solid fluxes and tube diameters, using grid-size dependent sub-grid models.
- Examine the effects of grid size on predicted flow behavior in the entrance and exit regions. Assess if the sub-grid model should be modified for rapidly accelerating flows, and improve the sub-grid model accordingly.
- Examine how particle size distribution affects the flow characteristics.

3.2) Implement sub-grid models for dispersion of mass and heat in MFIX and perform coarse-grid simulation of a reacting flow example in riser or a fluidized bed to demonstrate capability.
3.3) Perform coarse-grid simulation of flow in a simple CFB loop to demonstrate capability.

Coarse-grid Simulation of Gas-Particle Flows in Vertical Risers

Arthur T. Andrews IV, Peter N. Loezos and Sankaran Sundaresan*

Princeton University

Princeton, New Jersey

Submitted for Publication to Journal of Fluid Mechanics

January 2004

Keywords: riser flow, gas-particle flow, kinetic theory, CFD, sub-grid model, simulation

*Address correspondences to Sundaresan: sundar@princeton.edu

Abstract

It is well known that continuum model equations for unsteady gas-particle flows in devices such as fluidized beds and circulating fluidized bed risers contain unstable modes whose length scale is of the order of ten particle diameters. Yet, because of limited computational resources, these flows are routinely simulated by solving the discretized version of continuum models over coarse spatial grids. These simulations resolve the large-scale flow structures, but not the finer scale structures. In most industrial applications involving large devices, it is impractical to resolve all the fine-scale structures and therefore the effects of the unresolved structures must be addressed through suitable sub-grid models. Using gas-particle flows in a wide and very tall vertical channel as an example, we have demonstrated in this study that the results obtained in coarse-grid integration of the microscopic equations for gas-particle flows change appreciably if sub-grid corrections to account for the effects of unresolved structures are included. The addition of a simple time-averaged sub-grid model for the effective drag coefficient, and particle phase viscosity and pressure led to a qualitative change in the simulation results. Our simulations revealed a lack of separation of time scales between the resolved and unresolved structures. This led us to formulate a stochastic sub-grid model for the drag coefficient and investigate its consequence. The addition of a stochastic correction made quantitative, but not qualitative, changes to the simulation results.

Introduction

It is well known that gas-particle flows in vertical risers are inherently unstable, and that they manifest fluctuations over a wide range of length and time scales. There is a substantial body of literature where researchers have sought to capture these fluctuations through numerical simulation of continuum equations for gas-particle flows (Benyahia *et al*., 2000, 2002; Ding & Gidaspow, 1990; Enwald *et al*., 1997, 1999; Enwald & Almstedt, 1999; Nieuwland *et al*., 1995, 1996; Gidaspow, 1994; Lu & Gidaspow, 2003; Golschmidt *et al*., 2001; Neri & Gidaspow, 2000; Samuelsberg & Hjertager, 1996; Sun & Gidaspow, 1999; Tsuo & Gidaspow, 1990; van Wachem *et al*., 2001; Zhang & VanderHeyden, 2001). It is well known that continuum models for such flows, coupled with either simple phenomenological closures for drag and effective stresses (Glasser et al., 1998) or closures obtained by extending the kinetic theory of granular materials to account for the presence of the interstitial fluid (Gidaspow, 1994; Koch & Sangani, 1999; Agrawal *et al*., 2001), reveal unstable modes whose length scale is as small as ten particle diameters. Yet, because of limited computational resources, riser flows in large units are routinely simulated by solving discretized versions of the continuum models over a coarse spatial grid. Such coarse grid simulations do not resolve the small-scale spatial structures which, according to the continuum equations, do indeed exist. The accuracy of these simulation results is therefore questionable (Sundaresan, 2000). Such unresolved structures commonly arise in single phase turbulent flow, where large eddy simulations strive to incorporate the influence of the unresolved structures on those resolved in the simulations through sub-grid models; however, such sub-grid corrections have not received much attention in the context of heavily loaded gas-particle flows. Our study is aimed at

exposing the most important ingredients of sub-grid models for coarse-grid simulation of typical circulating fluidized bed riser flows.

Agrawal *et al*. (2001) have examined in detail the fate of a uniform suspension of particles fluidized by a gas through highly resolved simulations of continuum model equations in two-dimensional and three-dimensional periodic domains, whose size is of the order of the typical grid sizes employed in coarse-grid simulation of large scale risers and fluidized beds. In their analysis, they employed a kinetic theory closure for the particle phase stress (Lun *et al*., 1984; Gidaspow, 1994; Koch & Sangani, 1999), and a drag force model proposed by Wen & Yu (1966). They found that the uniformly fluidized state was unstable and that it quickly gave way to persistent, time-dependent, mesoscale structures, which assumed the form of clusters and streamers at low particle volume fractions and bubbles at high particle loadings. They found that the effective drag coefficient obtained by averaging the results over the periodic domain (a) was appreciably smaller than that corresponding to a homogeneous state, (b) was dependent on the size of the domain and (c) manifested a rather complex, but understandable dependence on particle volume fraction. They also found that the effective viscosity of and the normal stresses in the particle phase obtained by averaging over the mesoscale structures were (a) appreciably larger than those corresponding to the homogeneously fluidized state (given by the kinetic theory), and (b) depended on the size of the domain. Based on these findings, they concluded that unresolved mesoscale structures could contribute appreciably to results predicted by coarse-grid simulations.

The purpose of the present study is to investigate the influence of sub-grid models on the results obtained in coarse-grid simulations. We will demonstrate in this paper that

one must include sub-grid corrections (for drag coefficient and particle phase effective viscosity and pressure), and that because of a lack of separation of time scales between resolved and unresolved structures one should, in a strict sense, employ stochastic sub-grid models. However, simple deterministic sub-grid models seem to capture much of the large-scale flow structures obtained with stochastic sub-grid models.

It is appropriate to mention, at least in passing, that it has long been recognized in industrial practice that CFD simulations based on averaged equations of motion underestimate the holdup in fluidized beds and riser flows, unless an apparent particle cluster size, which is typically two to ten times the true size of the particles, is used in the calculations. Such a larger cluster size leads to a smaller drag coefficient than what would be obtained if the true particle size is employed. Thus, one can indeed view the use of an apparent particle cluster size as a simple sub-grid model for the drag coefficient. Apparent cluster size is sometimes used as a tuning parameter to match the simulation results with experimental data (e.g., see McKeen & Pugsley, 2003). A method to estimate the cluster size via an energy-minimization-multi-scale model, has been presented in the literature recently (Yang et al., 2003). Our study differs from these approaches in the sense that we have focused on identifying the relationship between the level of sophistication of the sub-grid models and the results obtained in coarse grid simulations.

Approach to coarse-grid simulations

The purpose of the simulations described in this study is to examine the flow behavior of a gas-particle suspension in a vertical channel, whose geometrical details are presented later. The starting point of the analysis is a kinetic theory based continuum model for gas-particle flow, see Table 1 (and appendix A for a brief description). A

detailed discussion of these equations can be found in Agrawal *et al*. (2001) and will not be repeated here. This model consists of continuity and momentum equations for the gas and particle phases, and an additional scalar equation for the fluctuation energy per unit mass of the particle phase. Henceforth, we will refer to these equations as microscopic (or kinetic theory) equations. Table 2 shows typical particle and gas properties. According to this system of microscopic equations, homogeneously fluidized suspensions (with properties shown in Table 2) are unstable with dominant instabilities occurring at a length scale of the order of ten particle diameters (Tan, 2000). We consider only those situations, where the dimensions of the riser are too large to make numerical simulations with grid sizes of the order of ten particle diameters impractical even in two-dimensional simulations. (Virtually every commercial or medium-scale pilot unit falls in this category.) Consequently, if one carries out coarse-grid integration of these microscopic equations employing a practically affordable grid resolution, there are bound to be small structures which have not been resolved and whose influence is not properly recognized in the simulations. This rather obvious point is well known in the literature on single-phase turbulent flow and turbulent flow with very dilute loading of particles. Yet, very little has been done about the sub-grid scale modeling in the context of densely loaded gas-particle flows. (In fact, the very need for sub-grid models has not been widely recognized and discussed.) In this manuscript we compare results obtained in simulation of the microscopic equations discretized using coarse grids with those obtained in coarse grid simulations where the microscopic equations have been augmented with sub-grid models of different levels of sophistication.[1]

[1] A question of fundamental importance in two-phase flows problems is the accuracy of the postulated microscopic equations in capturing the microscale physics behind the flow. The present study does *not*

Agrawal *et al*. (2001) have already pointed out that the origin of the small-scale structures in gas-particle flows through risers is very different from those in single-phase turbulent flow. In the latter, the small-scale eddies are dissipative and are largely sustained by energy cascade from larger eddies. In contrast, small-scale structures arise in riser flows primarily through local instabilities associated with fluidization; energy to sustain these structures comes largely from the mean relative motion between the particle and gas phases. Consequently, one should not directly apply the sub-grid models, which have been developed in single-phase turbulent flows, to the riser flow problem. Agrawal *et al*. (2001) proposed a simple, preliminary approach where highly resolved simulations of the microscopic equations are performed in small periodic domains which are commensurate with the grid sizes to be used in the coarse-grid simulations. This is precisely the approach we have examined here.

Although all the results will be presented in dimensionless form, it is useful to first present some quantities, such as riser dimensions and typical grid size that would be employed in coarse grid simulations, to motivate the specific combination of dimensionless variables employed in our test simulations. The vertical channel through which the gas-particle mixture flows is 76 cm wide and 30 m tall. In the coarse-grid simulation of flow described in this manuscript, the riser is discretized using 2 cm x 8 cm grids. These are fairly typical of industrial scale risers whose diameters range from 0.5 – 2.0 m and height ranges from 20 – 90 m. Three-dimensional simulations invariably employ even coarser grids.

---

address this question. Instead, we begin with a reasonable set of microscopic equations developed in the literature, which captures the known instabilities in simple test problems, and examine issues associated with the integration of this *given* set of equations using coarse grids.

The microscopic equations were made dimensionless using particle density (ρ_s), terminal velocity $\left(v_t\right)$ and $\left(\frac{v_t^2}{g}\right)$ as characteristic density, velocity and length (as in Agrawal *et al*., 2001). The particle size then appears in the microscopic equations as $\frac{dg}{v_t^2}\left(=\frac{1}{Fr_p}\right)$. The aspect ratio of the grid, vertical height $\left(\Delta_v\right)$ / horizontal width $\left(\Delta_h\right)$, is A. The width of the grid in dimensionless form is $\frac{\Delta_h g}{v_t^2}\left(=\frac{1}{Fr_h}\right)$. Using the dimensional quantities presented above as an illustration, A = 4, Fr_p ~ 65 and Fr_h ~ 0.2434. The larger the difference between Fr_p and Fr_h, the more important the contributions of the sub-grid corrections will be. Indeed, Agrawal et al. (2001) found that as Fr_h decreased, the effects of the mesoscale structures assumed greater and greater importance.

Table 1: MODEL EQUATIONS FOR GAS-PARTICLE FLOWS

$$\frac{\partial \phi}{\partial t} + \nabla \cdot (\phi \underline{v}) = 0 \tag{1}$$

$$\frac{\partial (1-\phi)}{\partial t} + \nabla \cdot \left[(1-\phi) \underline{u} \right] = 0 \tag{2}$$

$$\left[\frac{\partial (\rho_s \phi \underline{v})}{\partial t} + \nabla \cdot \left(\rho_s \phi \underline{v} \underline{v} \right) \right] = \quad -\nabla \cdot \underline{\underline{\sigma}}_s \quad - \quad \phi \nabla \cdot \underline{\underline{\sigma}}_g \quad + \quad \underline{f} \quad + \quad \rho_s \phi \underline{g} \tag{3}$$

$$\left[\frac{\partial \left(\rho_g (1-\phi) \underline{u} \right)}{\partial t} + \nabla \cdot \left(\rho_g (1-\phi) \underline{u} \underline{u} \right) \right] = \quad -(1-\phi) \nabla \cdot \underline{\underline{\sigma}}_g \quad - \quad \underline{f} \quad + \rho_g (1-\phi) \underline{g} \tag{4}$$

$$\left[\frac{\partial \left(\frac{3}{2} \rho_s \phi \Theta \right)}{\partial t} + \nabla \cdot \left(\frac{3}{2} \rho_s \phi \Theta \underline{v} \right) \right] = \quad -\nabla \cdot \underline{q} \quad - \quad \underline{\underline{\sigma}}_s : \nabla \underline{v} \quad + \Gamma_{slip} \quad - \quad J_{coll} \quad - \quad J_{vis} \tag{5}$$

Gas phase stress tensor

$$\underline{\underline{\sigma}}_g = p_g \underline{\underline{I}} - \hat{\mu}_g \left[\nabla \underline{u} + (\nabla \underline{u})^T - \frac{2}{3} (\nabla \cdot \underline{u}) \underline{\underline{I}} \right] \tag{6}$$

Gas-particle drag (Wen & Yu, 1966; Gidaspow, 1994)

$$\underline{f} = \beta (\underline{u} - \underline{v}) \;\; ; \;\; \beta = \frac{3}{4} C_D \frac{\rho_g (1-\phi) \phi \left| \underline{u} - \underline{v} \right|}{d} (1-\phi)^{-2.65} \tag{7}$$

$$C_D = \begin{cases} \dfrac{24}{Re_g} \left(1 + 0.15 Re_g^{\,0.687} \right) & Re_g < 1000 \\ 0.44 & Re_g \geq 1000 \end{cases} \quad ; \quad Re_g = \frac{(1-\phi) \rho_g d \left| \underline{u} - \underline{v} \right|}{\mu_g}$$

Table 1 – continued

Particle phase stress

$$\underline{\underline{\sigma_s}} = \left[\rho_s \phi \left(1 + 4\eta\phi g_o\right)\ \mathrm{T} - \eta\mu_b \left(\nabla \cdot \underline{\mathrm{v}}\right)\right]\ \underline{\underline{\mathrm{I}}}$$
$$-\left(\frac{2+\alpha}{3}\right)\left\{\frac{2\mu^*}{g_o\eta\left(2-\eta\right)}\left(1+\frac{8}{5}\phi\eta g_o\right)\ \left(1+\frac{8}{5}\eta\left(3\eta-2\right)\ \phi\ g_o\right)+\frac{6}{5}\eta\mu_b\right\}\underline{\underline{S}} \qquad (8)$$

where $\underline{\underline{S}} = \frac{1}{2}\left(\nabla\underline{\mathrm{v}} + \left(\nabla\underline{\mathrm{v}}\right)^{\mathrm{T}}\right) - \frac{1}{3}\left(\nabla\cdot\underline{\mathrm{v}}\right)\underline{\underline{\mathrm{I}}}$

$$\mu^* = \frac{\mu}{1+\dfrac{2\beta\mu}{\left(\rho_s\phi\right)^2 g_o \mathrm{T}}}\ ;\mu = \frac{5\rho_s d\sqrt{\pi\mathrm{T}}}{96}\ ;$$

$$\mu_b = \frac{256\mu\phi^2 g_o}{5\pi}\ ;\ \ \eta = \frac{\left(1+e_p\right)}{2}; g_o = \frac{1}{1-\left(\phi/\phi_{\max}\right)^{1/3}}\ ;\ \phi_{\max} = 0.65; \alpha = 1.6$$

Pseudo-thermal energy flux

$$\underline{\mathrm{q}} = -\frac{\lambda^*}{g_o}\left\{\left(1+\frac{12}{5}\eta\phi g_o\right)\ \left(1+\frac{12}{5}\eta^2(4\eta-3)\phi g_o\right)+\frac{64}{25\pi}\left(41-33\eta\right)\ \eta^2\phi^2 g_o^2\right\}\ \nabla\mathrm{T} \quad (9)$$

where $\lambda^* = \dfrac{\lambda}{1+\dfrac{6\beta\lambda}{5\left(\rho_s\phi\right)^2 g_o \mathrm{T}}}; \lambda = \dfrac{75\rho_s d\sqrt{\pi\mathrm{T}}}{48\eta\left(41-33\eta\right)}$

Rate of dissipation of pseudo-thermal energy through collisions

$$\mathrm{J}_{\mathrm{coll}} = \frac{48}{\sqrt{\pi}}\eta\left(1-\eta\right)\frac{\rho_s\phi^2}{\mathrm{d}} g_o \mathrm{T}^{3/2} \qquad (10)$$

Table 1 – continued

Effect of fluid on particle phase fluctuation energy (Koch & Sangani, 1999)

$$J_{vis} = \frac{54\ \phi\mu_g T}{d^2} R_{diss}, \quad \text{where}$$
$$R_{diss} = 1+\frac{3\phi^{1/2}}{\sqrt{2}}+\frac{135}{64}\phi\ln\phi+11.26\phi\ (1-5.1\phi+16.57\phi^2-21.77\phi^3)\text{-}\phi g_o \ln(0.01) \tag{11}$$

$$\Gamma_{slip} = \frac{81\phi\mu_g^2\left|\underline{u}-\underline{v}\right|}{g_o d^3\rho_s\sqrt{\pi T}}\Psi, \quad \text{where} \tag{12}$$

$$\Psi = \frac{R_d^2}{(1+3.5\phi^{1/2}+5.9\phi)},$$

$$R_d = \begin{cases} \dfrac{1+3(\phi/2)^{1/2}+(135/64)\phi\ln\phi+17.14\phi}{1+0.681\phi-8.48\phi^2+8.16\phi^3}, & \phi<0.4 \\ \dfrac{10\phi}{(1\text{-}\phi)^3}+0.7, & \phi\geq 0.4 \end{cases}$$

Table 2: Physical properties of gas and solids

d	particle diameter	7.5×10^{-3} cm
ρ_s	particle density	1.5 g/cm^3
ρ_g	Gas density	1.3×10^{-3} g/cm^3
μ_g	Gas viscosity	1.8×10^{-4} g/cm·s
e_p	Coefficient of restitution	0.9

Simulations to estimate sub-grid corrections

Agrawal *et al*. (2001) proposed that, as a preliminary approach to constructing sub-grid models, one perform highly resolved simulations of the microscopic equations in small periodic domains, whose dimensions are commensurate with the grid dimensions of the planned coarse-grid simulations. Such calculations begin with a uniformly fluidized suspension of particles, and simulate the evolution of non-uniform structures through instabilities inherent to the fluidization problem. Details of such simulations are described in Agrawal *et al*. (2001), and will not be repeated here. We simply note that the computations were performed using the MFIX code (Syamlal *et al*., 1993; Syamlal, 1998), which is based on discretization using staggered Cartesian grids and a finite volume method. Spatial and temporal derivatives were approximated using a second order discretization scheme and an implicit Euler scheme, respectively. As non-uniform structures evolve, the gas will bypass regions rich in particles, and the domain-averaged slip velocity between the gas and the particles (defined as the difference between domain average values of volume fraction-weighted gas and particle phase velocities) required to support the weight of the particles will take on a larger value than that for the uniformly fluidized state. The non-uniform structures are dynamic in nature, and so will the domain-average slip velocity be. This is illustrated in Figure 1, which presents the instantaneous domain-averaged dimensionless slip velocity as a function of dimensionless time in one such periodic domain calculation.

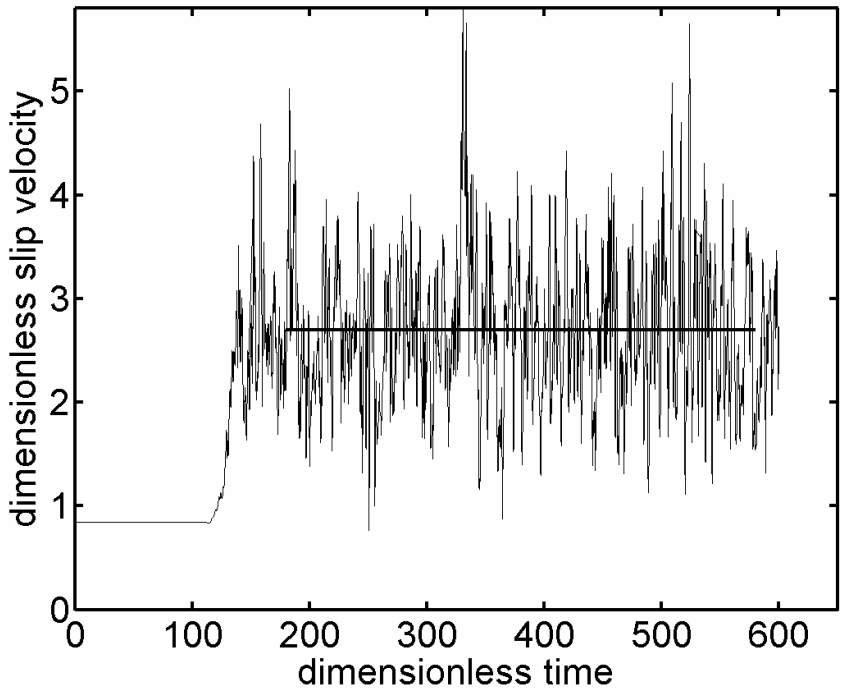

Figure 1 Domain-averaged dimensionless slip velocity calculated in a doubly periodic domain with $Fr_h = 0.2434$; A = 4; Average particle volume fraction in the domain = 0.05; Reynolds number based on particle diameter and terminal settling velocity, $Re_p = 1.18$. Highly resolved simulation of flow in this periodic domain was performed using 32 x 128 grids. Time-averaged slip velocity shown as a superimposed line, and was calculated between 200 and 800 dimensionless time units. The imposed shear rate in the periodic domain is zero. See Agrawal et al. (2001) for details on the introduction of macroscale shear in the periodic domain calculations.

In such simulations, the pressure drop across the bed is chosen to balance the weight of the suspension, and therefore the instantaneous domain-averaged dimensionless drag coefficient (defined such that the domain-averaged dimensionless drag coefficient multiplied by the domain-averaged dimensionless slip velocity is simply the effective

dimensionless drag force per unit volume in the domain[2]) can readily be extracted from the results shown in figure 1. It can be seen from figure 1 that after an initial transient period, the flow settles into a statistical steady state with persistent fluctuations. By averaging the results obtained in the statistical steady state, one can obtain a time-averaged value for the domain-averaged slip velocity (shown by the horizontal line in this figure) and then a corresponding time-averaged value for the domain-averaged drag coefficient. By repeating these simulations for different average particle volume fractions in the domain and imposed shear rates, one can create a look-up table or a simple curve-fit function for the time-averaged drag coefficient in terms of the average particle volume fraction and dimensionless shear rate. We found the shear dependence of the effective drag coefficient to be weak for typical shear rates encountered in riser flows, so that the effective drag coefficient is simply taken as a function of the particle volume fraction in the domain. This function will change with Fr_h; however, the value of Fr_h was not changed in our simulations. Agrawal *et al*. (2001) found that the domain-averaged quantities had only a weak dependence (if any) on A, for $A > \sim 4$. In all our coarse grid simulations, A was four.

[2] More elaborate descriptions of effective interphase interaction force that includes dynamic effects (Zhang & Vanderheyden, 2002) or drift velocity correction (Deutsch & Simonin, 1991) are not considered in the present analysis.

Agrawal *et al*. (2001) proposed the use of the look-up table or the curve-fit function for the effective (time-averaged) drag coefficient discussed in the previous paragraph in coarse-grid simulations, as a simple model for the effect of the unresolved structures on the interphase interaction force. We have examined the impact of such a sub-grid model for drag coefficient in our coarse-grid simulations (described later). Such an approach has its limitations; for example, its validity in the vicinity of boundaries such as solid walls is arguable. Nevertheless, we have applied a sub-grid model generated through this approach everywhere in the flow domain, as fluctuations in gas-particle flows in risers do not appear to be driven by shear at bounding surfaces – more on this later.

Note that the instantaneous domain-averaged slip velocity, and hence the instantaneous domain-averaged drag coefficient, fluctuate with time, and the basis for using time-averaged values for these quantities to construct a sub-grid model is reasonable if and only if the characteristic fluctuation time scale observed in the coarse-grid simulation is much larger than that in the sub-grid calculations illustrated in figure 1. When a clear separation of time scales does not exist, the consequences of the fluctuating drag coefficient seen in the statistical steady state (illustrated in figure 1) should be brought into the coarse-grid simulations. We will however, begin with time-averaged sub-grid models and evaluate if a separation of time scale exists or not.

As discussed in detail by Agrawal *et al*. (2001), one can also extract effective particle phase normal stresses in the vertical and lateral directions, and effective particle phase viscosity from such highly resolved simulations. Once again, one can raise the issue as to whether time-averaged sub-grid models for these quantities (which take the

form of look-up tables or curve-fit functions) are adequate if there is no clear separation of time scales.

Table 3 contains the time-averaged sub-grid models for the specific values of Fr_h and A used in our illustrative examples[3]. The effective dimensionless drag coefficient, $\overline{\beta}$, is simply a function of local particle volume fraction, i.e. $\overline{\beta} = \overline{\beta}(\phi)$, where ϕ is the instantaneous volume fraction of particles at any node in the coarse grid simulation (and equal to the average volume fraction of particles in the domain in the sub-grid model calculations described in this section). The time-averaged dimensionless sub-grid horizontal normal stress and effective sub-grid particle phase viscosity ($P_{s,meso}$ and $\mu_{s,meso}$, respectively) depended both on ϕ and the prevailing macroscale shear rate (see expressions in Table 3, where $|\tilde{\gamma}|$ denotes the absolute value of the dimensionless shear rate). Both of these quantities decreased with increasing shear rate, indicating a tendency of the shear to orient the clusters and hinder their lateral fluctuations. This shear dependence is exactly opposite of what one obtains in single-phase turbulent flows where sub-grid viscosity and stresses increase with shear rate. The contribution of the vertical normal stress in riser flow simulations is, in general, a very small correction to the convective momentum flux, and hence can be ignored with little loss of accuracy.

[3] The expressions described here are simple *ad hoc* sub-grid models. Fundamentally based models for the sub-grid corrections are certainly more desirable and should be developed. However, we have not embarked on such a task yet; here, we simply focus on demonstrating the significant difference introduced into the results when sub-grid models are added, thus making a case for sub-grid models.

Table 3: Computationally generated *ad hoc* sub-grid model for various dimensionless quantities

---

$$P_{s,meso} = 1.54\exp(-.701|\tilde{\gamma}|)\phi$$

$$\mu_{s,m_{eso}} = \begin{cases} \left(0.0121|\tilde{\gamma}|^3 - 0.0605|\tilde{\gamma}|^2 + 0.0314|\tilde{\gamma}| + .130\right)\dfrac{\phi}{0.398} & \text{for} \quad |\tilde{\gamma}| < 2.45 \\ 0.0546\phi \quad \text{for} \quad |\tilde{\gamma}| \geq 2.45 \end{cases}$$

$$\overline{\beta} = \left(1 - \frac{\rho_g}{\rho_s}\right)\frac{\phi(1-\phi)}{F}, \text{ where}$$

$$F = \begin{cases} \left(396\phi^2 - 30.8\phi + 1\right) & \text{for} \quad \phi < 0.0375 \\ \left(.151\ln(\phi) + .898\right) & \text{for} \quad \phi \geq 0.0375 \end{cases}$$

Coarse-grid simulations of riser flow

We have performed two-dimensional[4] coarse-grid simulations of gas-particle flows in a vertical channel equipped with a horizontal splash plate at the top, shown schematically in figure 2. Gas and particles entered the channel at the bottom and exited through two symmetric openings on the sides, located near the top of the riser. The gas and particle velocities at the inlet were independent of lateral position, and equal to 27.47 and 16.67 dimensionless units, respectively. The aspect ratio of the grids used in the coarse grid simulations was 4, and the Froude number based on the grid width, Fr_h, was 0.2434. These are exactly the same as the values of A and Fr_h used in the sub-grid model calculations outlined in the previous section.

The coarse-grid simulations employed the effective drag coefficients determined from the sub-grid calculations. We have simply used the sub-grid model for the horizontal normal stress as the effective mesoscale pressure model, i.e. the anisotropy in the horizontal and vertical sub-grid normal stresses was ignored. This particular choice is a reasonable first approximation as the influence of the effective particle phase normal stress is unimportant in the vertical momentum balance. [In the cases simulated, the contribution from the gas phase deviatoric stress is negligible when compared to that due to the particle phase. Therefore, we did not include any sub-grid correction for the gas phase viscosity and simply assumed that the effective viscosity of the gas phase was equal to that of the gas itself.]

[4] While 3 – D simulations are more desirable, the computational costs are prohibitive. Unlike single phase turbulent flow, nonuniform structures in the gas-particle flow studied here arise primarily through local instabilities, which are already captured in 2 – D analysis. Indeed, Agrawal et al. (2001) have shown that both 2 – D and 3 – D simulations of flows in small periodic domains yield similar results, so that there is some reason to hope that the 2 – D and 3 – D coarse-grid simulations will also lead to similar findings.

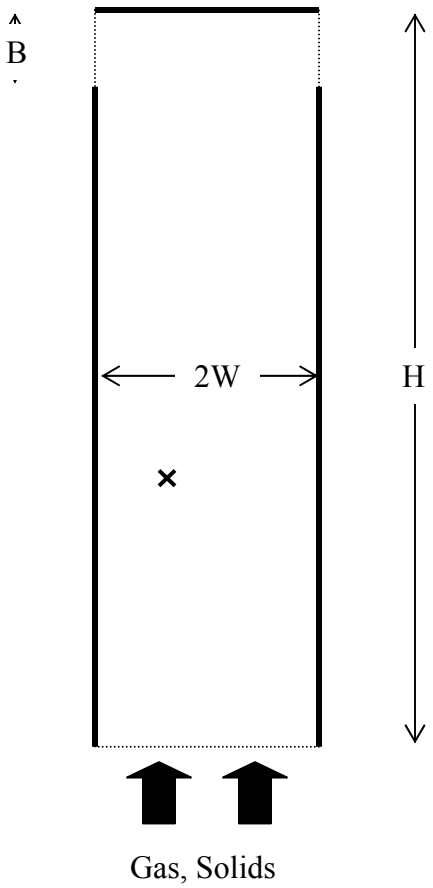

Figure 2: Schematic diagram showing the geometry used in 2D coarse grid simulations. Riser half-width, W = 78.1; Riser height, H = 6164; Exit opening height, B = 102.7 (all in dimensionless units). Volume fraction of particles at the inlet = 0.04. Simulations were done using 38 x 375 grids. The location designated by "X" will be referred to later.

Very little is known about appropriate wall boundary conditions in *coarse-grid* simulations of densely loaded gas-particle flows. In high-velocity flows of densely loaded gas-particle mixtures through vertical pipes, the shear stress transmitted through the particle phase is generally much larger than that due to the gas; indeed, numerical experiments suggest that there is hardly any difference between results obtained with no-slip and free-slip boundary conditions for the gas phase. Thus, in the class of problems addressed here, the gas phase boundary condition at the walls is not a critical factor.

Visual observations of flows through vertical pipes indicate that particles do slip near the wall, and hence a partial or free-slip boundary condition for the particle phase is indicated. It is generally believed that in high-velocity flows of densely loaded gas-particle mixtures through large risers the vertical pressure gradient is largely due to the particle holdup and that wall shear is only weakly relevant (Chang & Louge, 1992). Thus, the correct boundary condition for the large channel flow problem studied here is quite possibly a partial-slip condition, which is not far from a free-slip boundary condition. In the simulations described in this manuscript, we have examined both no-slip and free-slip boundary conditions for the particle and gas-phases at the bounding walls. These two extremes serve as bounds (within which the true boundary condition should lie) and thus give an idea about the extent of the changes in the mean flow characteristics that can come about upon altering the boundary conditions. It also helps us assess whether the need for (and the influence of) sub-grid models is dependent on the wall boundary conditions employed.

Agrawal *et al*. (2001) noted that the kinetic theory stresses were dwarfed by the mesoscale corrections when Fr_p exceeded Fr_h by a factor of ~100, which was indeed the case here. Consequently, one need not consider the fluctuation energy equation at all in the coarse-grid simulations. We examined the effect of including the fluctuation energy equation in our coarse-grid simulations and found that the kinetic theory stresses were indeed small. [Strictly speaking, if one wants to retain the fluctuation energy equation, sub-grid models for the various terms appearing in this equation must be constituted, which was not done in the present study. In our simulations, we used the effective sub-grid particle phase viscosity in the shear production of fluctuation energy.]

The coarse-grid simulation was always carried out for a long duration (typically several thousand units of dimensionless time) and a statistical steady state was allowed to establish itself before data on various flow characteristics were gathered. The time-averaged data presented here were obtained by averaging the simulation results over ~ 3000 dimensionless units of time.

Figures 3a and 3b show the time dependence of the slip velocity between the gas and particle phases and the particle volume fraction at an arbitrarily chosen location in the riser. This location, marked as X in figure 2, is 86.3 dimensionless units of length away from the left side riser wall and at an elevation of 2301 dimensionless units of length from the bottom inlet. As expected, persistent fluctuations in all the dependent variables were observed throughout the riser – figures 3a and 3b are simply typical examples. Figure 3c shows the power spectrum corresponding to the results shown in figure 3a. Although a single dominant frequency could not be identified from this figure, the range of frequencies over which most of the fluctuations occurred in the coarse-grid simulations could readily be identified. Very similar results were obtained in coarse-grid simulations using free-slip boundary conditions. Thus, the fluctuations seen here are not due to the same mechanism that drives turbulent pipe flow of a single-phase fluid.

In order to examine if there was indeed a separation of time scale between the sub-grid scale simulations (figure 1) and the coarse-grid scale simulations (figure 3), we present in figure 4 further details of a representative sub-grid scale simulation. The simulation conditions are exactly as in figure 1. Figure 4a shows the instantaneous domain-averaged drag coefficient (related inversely to the slip velocity shown in figure 1) as a function of dimensionless time. The characteristic time used to make the results

dimensionless is exactly the same in sub-grid and coarse-grid simulations. Figure 4b shows the power spectrum corresponding to figure 4a. It is readily apparent from a comparison of figures 3b and 4b that the range of dimensionless frequencies is comparable in both cases. Thus, there is no basis for ignoring in the coarse-grid simulations the fluctuations in the sub-grid drag coefficient. In other words, the use of a time-averaged sub-grid model for effective drag coefficient is, in a formal sense, not warranted.

This lack of separation of time scales suggests that the fluctuations observed in the sub-grid and coarse-grid simulations are driven by the same mode of instability. Given that the sub-grid scale simulations considered only the fluidization instability, it is reasonable to attribute the persistent fluctuations seen in the coarse-grid simulations to a local instability associated with particle phase inertia, gravity and the dependence of the drag coefficient on particle volume fraction. In this physical picture, small-scale structures arise as a result of local instabilities and coalesce to produce large scale fluctuations observed in coarse-grid simulations.

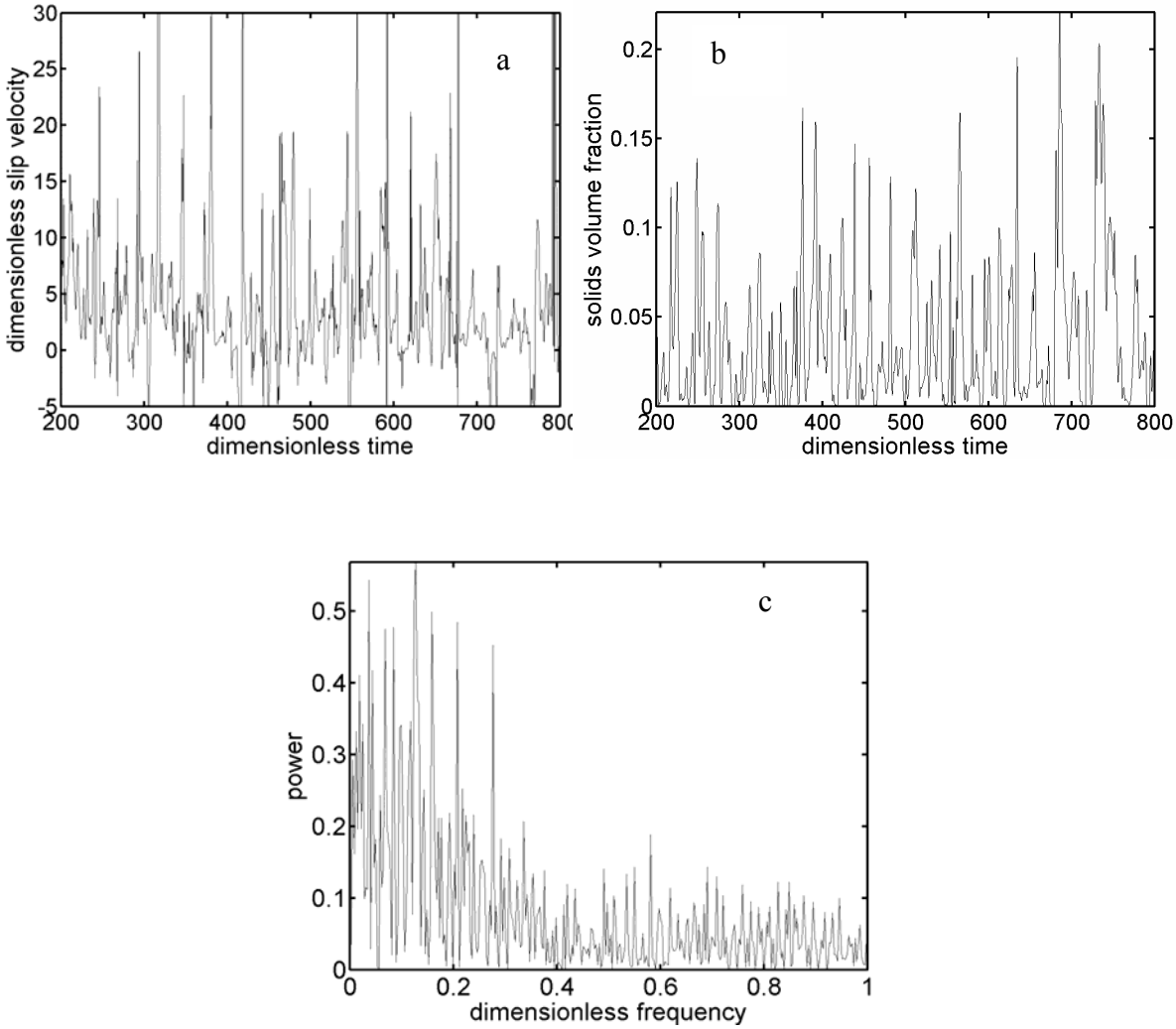

Figure 3: Results obtained from a coarse grid simulation with time-averaged sub-grid models for drag coefficient and the stresses. (a) Dimensionless slip velocity and (b) particle volume fraction as functions of dimensionless time at the location marked as X in figure 2. (c) The corresponding power spectrum.

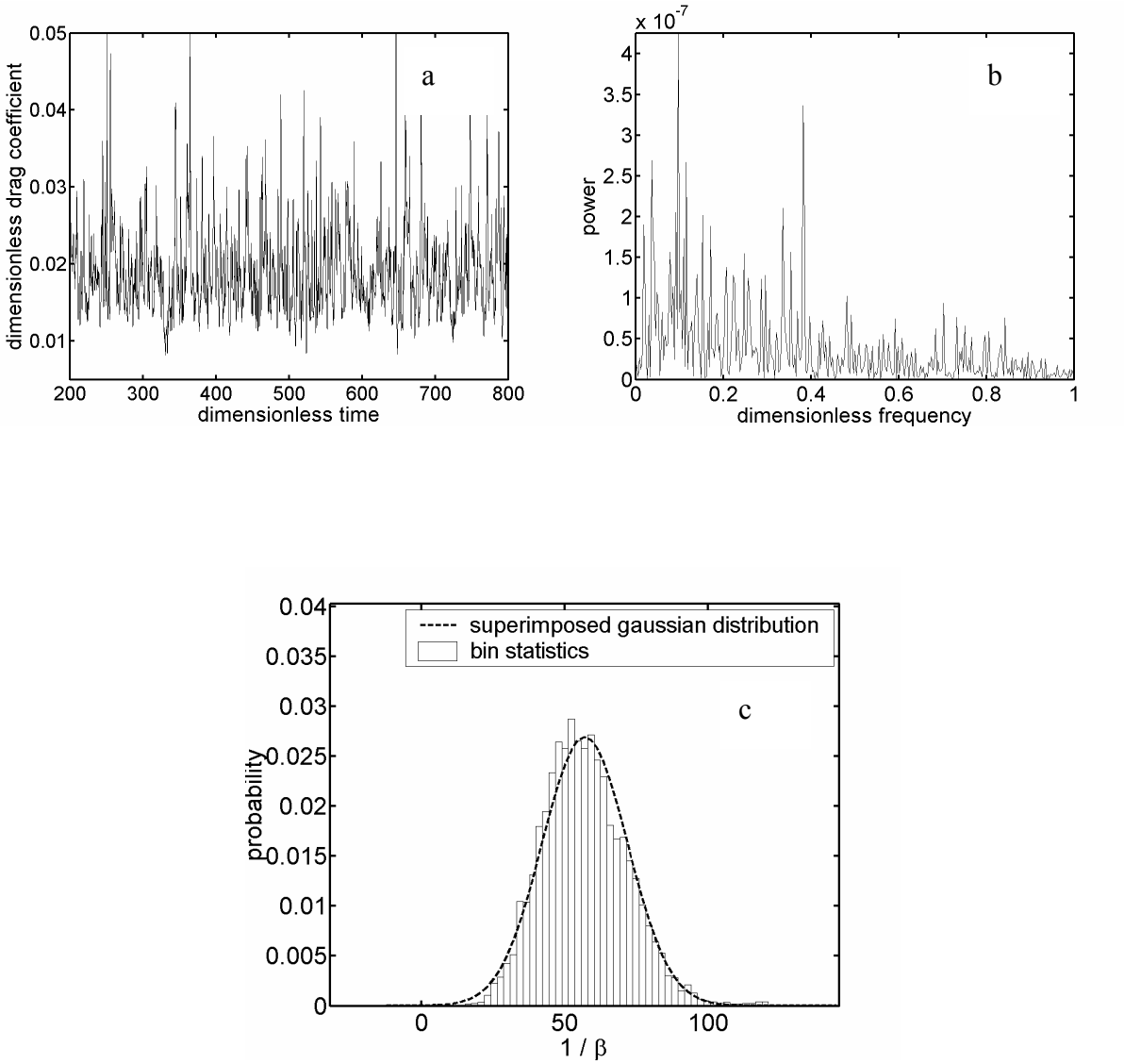

Figure 4: (a) Dimensionless drag coefficient, β_{meso}, vs. dimensionless time. (b) Power spectrum corresponding to figure 4a. (c) Probability distribution function vs. ($1 / \beta_{meso}$) corresponding to figure 4a. Geometry and conditions are the same as in figure 1.

In sub-grid simulations (such as those shown in figures 1 and 4), mesoscale structures are repeatedly formed and destroyed, and the fluctuations in the slip velocity (and other mesoscale quantities) are tied to the fluctuations in the configuration of the mesoscale structure. Thus, the need to include the effect of sub-grid drag coefficient fluctuations in the coarse-grid simulations can be interpreted as a need to recognize the fact that the instantaneous sub-grid mesoscale structure can vary about a mean configuration. It then follows that a proper sub-grid model for the fluctuations should try to capture the evolution of the sub-grid structure. As this structure is being convected by flow, it is reasonable to anticipate that a full-fledged sub-grid model for the fluctuations should be a dynamic model including convective derivatives. Such a dynamic model is rather complex and we have not pursued it in the present study. Instead, we consider a very simple localized sub-grid model that treats the fluctuations in the effective drag coefficient (see figure 4a) as a random stochastic event.

Figure 4c shows that the probability distribution function for $\left(1 \big/ \beta_{meso} \right)$ in the statistical steady state, corresponding to the results presented in figure 4a, is essentially Gaussian. This suggests that, as a simple approximation, one can write

$$\left(\frac{1}{\beta_{meso}} \right) = \left(\frac{1+f}{\bar{\beta}} \right)$$

where f is a zero-mean Gaussian random variable with suitably chosen variance, and $\overline{\beta}$ is the average drag coefficient shown in figure 4a by the horizontal line. The line shown in figure 4c confirms that such a functional representation does capture the pdf.

Stochastic sub-grid model

In order to examine the possible consequence of a lack of separation of time scales between the coarse-grid and sub-grid fluctuations, we constructed a simple time-dependent sub-grid model for the effective drag coefficient. Accordingly, the drag coefficient at each node of the coarse-grid simulation was treated as an independent stochastic random variable modeled via an Uhlenbeck-Ornstein (1930) process. Thus, the instantaneous drag coefficient, $\beta_{meso,j}(t)$, of the jth node was written as

$$\left(\frac{1}{\beta_{meso,j}}\right)=\left(\frac{1+f_j(t)}{\overline{\beta}\left(\phi_j(t)\right)}\right)$$

where $\phi_j(t)$ is the instantaneous particle volume fraction at that node, $\overline{\beta}$ is the sub-grid model for the time-averaged drag coefficient and f_j is a stochastic random variable with zero-mean. The Uhlenbeck-Ornstein (U-O) model to evolve a stochastic random variable f can be summarized as follows.

If f_t denotes the value of a random variable f at time t, its value at time $t+\Delta t$, $f_{t+\Delta t}$, is set to be $f_{t+\Delta t}=(\alpha_1)f_t+(\alpha_2\sigma)Rn$, where $\alpha_1=\exp(-\Delta t/\tau^*)$ and $\alpha_2=\sqrt{1-\alpha_1^2}$. Here τ^* and σ are model parameters; Rn is a random number with a Gaussian distribution, $\langle Rn\rangle=0$, and $\langle Rn^2\rangle=1$. The random variable f, evolved in time

according to this rule, satisfies $\langle f \rangle = 0, \left\langle f^2 \right\rangle = \sigma^2$ and $\left\langle f_t f_{t+\Delta t} \right\rangle = \sigma^2 \exp(-\Delta t / \tau^*)$, where $\langle\ \rangle$ denotes time averaging.

Figure 5 illustrates the stochastic sub-grid model for drag coefficient, applied to the conditions simulated earlier in figure 4. It is remarkable that the simple U-O process produces fluctuations similar to those seen in the detailed sub-grid scale flow simulations. Thus, it is reasonable to hope that such a stochastic sub-grid model for the drag coefficient can be used as a simple vehicle to investigate the possible effect of a lack of separation of time scale between the sub-grid and coarse-grid simulations. We found that the standard deviation σ and the characteristic time τ^* (which were extracted from our meso-scale simulations) varied somewhat with particle volume fraction. However, for the sake of simplicity, we have assumed in the coarse-grid simulations described below that they are approximately constant [$\sigma = 0.25$; $\tau^* = 1.12$, both being dimensionless].

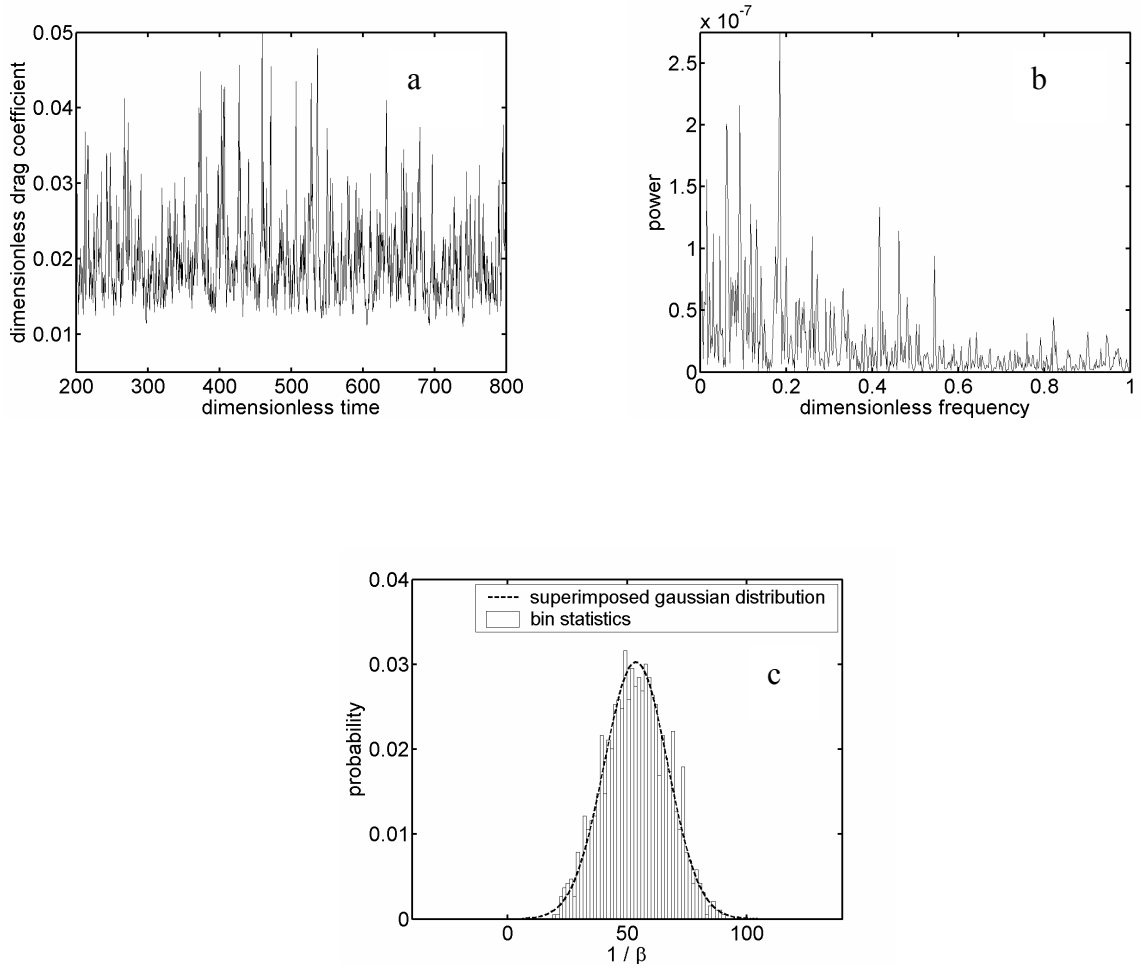

Figure 5: Temporal fluctuations in drag coefficient modeled as a Uhlenbeck-Ornstein process. U-O model parameters: characteristic time, $\tau^* = 1.12$ dimensionless time units; $\sigma = 0.25$. Particle volume fraction = 0.05. The time-averaged drag coefficient is set to be same as that in figure 4a. (a) Dimensionless drag coefficient, β_{meso}, vs. dimensionless time. (b) Power spectrum corresponding to figure 5a. (c) Probability distribution function vs. ($1/\beta_{meso}$) corresponding to figure 5a.

In what follows, when we talk about coarse-grid simulations with a *stochastic* sub-grid model for riser flows, we refer to coarse-grid simulations employing a stochastic sub-grid model for the drag coefficient along with time-averaged sub-grid models for particle-phase pressure and viscosity. We focused primarily on the drag coefficient, as the interphase interaction force term, particle inertia and the gravitational force term are the most dominant terms in the vertical momentum balance. Similarly, when we discuss coarse-grid simulations using a *time-averaged* sub-grid model, we refer to coarse-grid simulations employing time-averaged sub-grid models for the drag coefficient, and particle-phase pressure and viscosity. Finally, coarse-grid simulations with *no* sub-grid model refer to results obtained by simply solving the microscopic equations (kinetic theory model) on a coarse grid without including any sub-grid correction.

Coarse-grid simulations with different sub-grid models

We repeated the coarse-grid simulation described earlier in figures 2 and 3, using the stochastic sub-grid model. We also performed an identical simulation where no sub-grid corrections were made. Figures 6a – 6c obtained with the stochastic sub-grid model are analogous to figures 3a – 3c discussed earlier in the context of time-averaged sub-grid model.

It is clear that the addition of a stochastic fluctuation in the drag coefficient has not produced any qualitative difference in the fluctuations. Instantaneous snapshots of particle volume fraction profiles between these two models also appeared qualitatively similar – compare figures 7a and 7b. The same was true for the velocity fields as well. Thus, no qualitatively new feature appeared in the simulation results because of the addition of the stochastic correction.

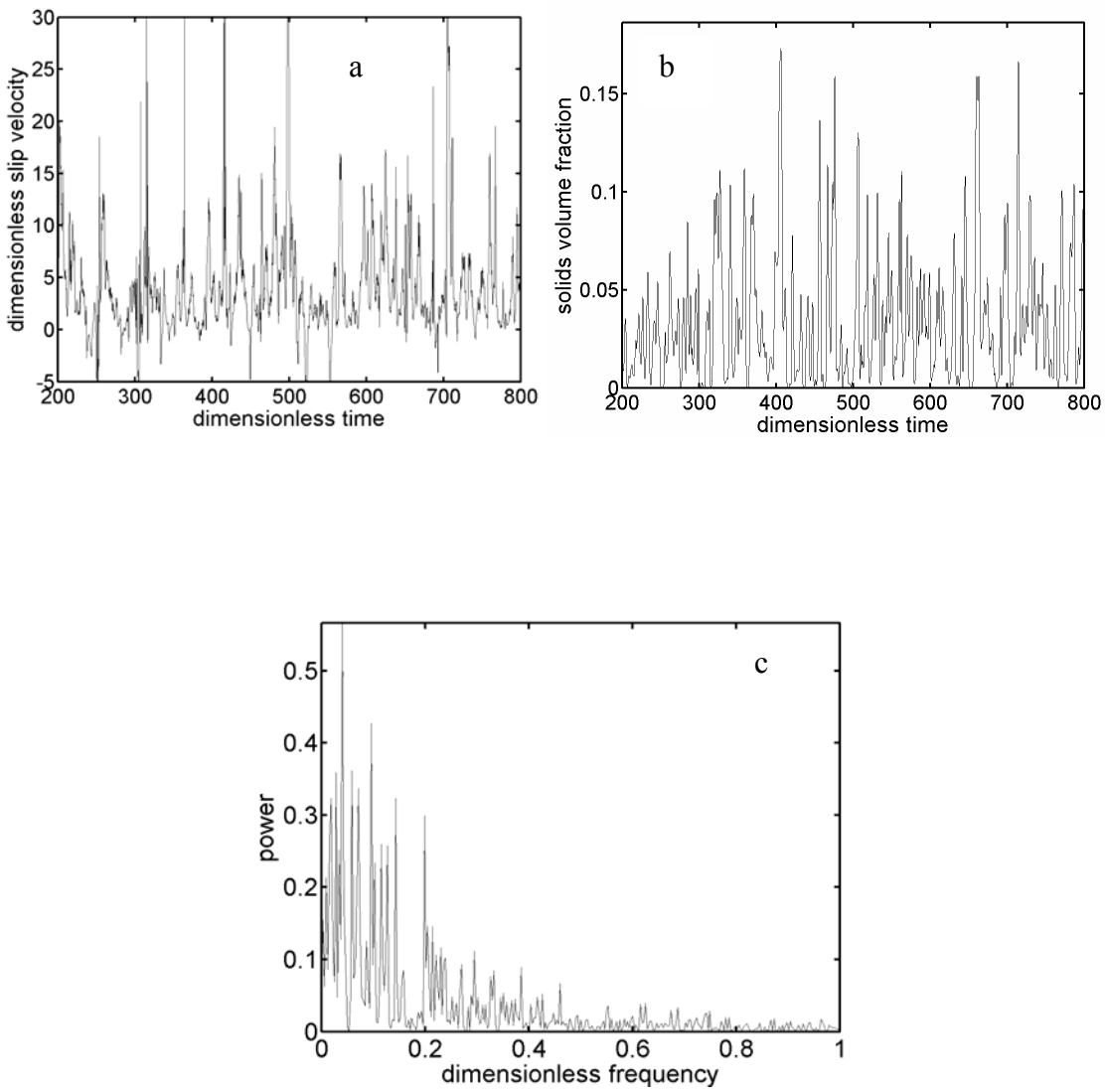

Figure 6: Results obtained from a coarse grid simulation with stochastic sub-grid model for drag coefficient and time-averaged sub-grid models for the stresses. (a) Dimensionless slip velocity and (b) particle volume fraction as functions of dimensionless time at the location marked as X in figure 2. (c) The corresponding power spectrum.

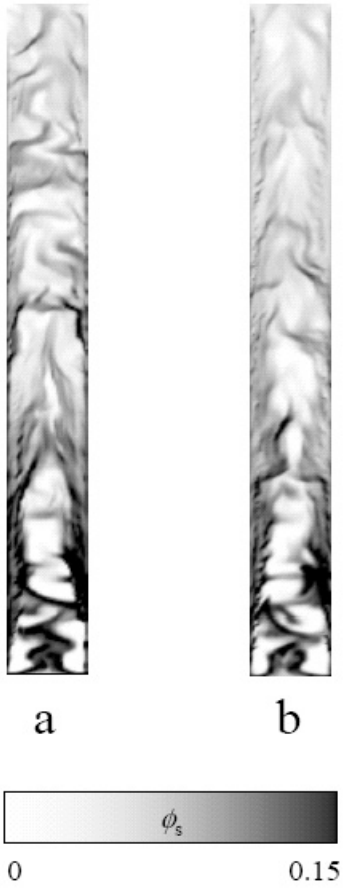

Figure 7: Snapshots of particle volume fractions obtained in the coarse-grid simulations. (a) Time-averaged sub-grid model, (b) stochastic sub-grid model. No-slip boundary conditions for both phases.

Surprisingly, however, when no-sub-grid model was included, large-scale nonuniformities could not be sustained even if we began our simulations with highly nonuniform initial conditions in the riser. For example, we carried out coarse-grid simulations using a stochastic sub-grid model and allowed a statistical steady state to evolve. We then stopped the simulation at different times in the statistical steady state, turned off the sub-grid model, and continued the simulation. We found that over a few multiples of the residence time in the riser the inhomogeneities washed out of the riser

and a nearly homogeneous state with small fluctuations resulted. Thus, in this example, inhomogeneities could not be sustained without adding sub-grid models.

From our coarse-grid simulations, we have obtained the time-averaged profiles of various quantities in the statistical steady state, some of which are illustrated below. Figure 8 shows the laterally averaged particle volume fraction as a function of riser elevation for the three cases: no sub-grid, time-averaged sub-grid, and stochastic sub-grid models. We performed simulations with two different initial conditions, one where the channel was initially devoid of particles and another where the channel was initially filled with a non-uniform distribution of particles. The time-averaged results representing a statistical steady state showed no significant dependence on the initial condition. (Some small difference was invariably present; however, as the difference decreased with increasing sampling time, it was taken as an indication that the data had not been averaged for a sufficiently long duration.)

The result obtained in the *no sub-grid model* case is qualitatively different from those in the other two cases. It proved to be deficient in the sense that it did not reproduce the generally known, large scale fluctuations. The axial profiles for the other two cases manifest peaks in the laterally averaged particle volume fraction at an intermediate elevation in the riser (~ 15% of riser height from the bottom). In simulations with both the time-averaged and stochastic sub-grid models, particle rich regions are more commonly seen near the wall, and they slowly descend, causing an accumulation near the bottom of the riser. However, the upward flow from the inlet tends to push the accumulated solids upwards, and these two opposing effects may be responsible for the

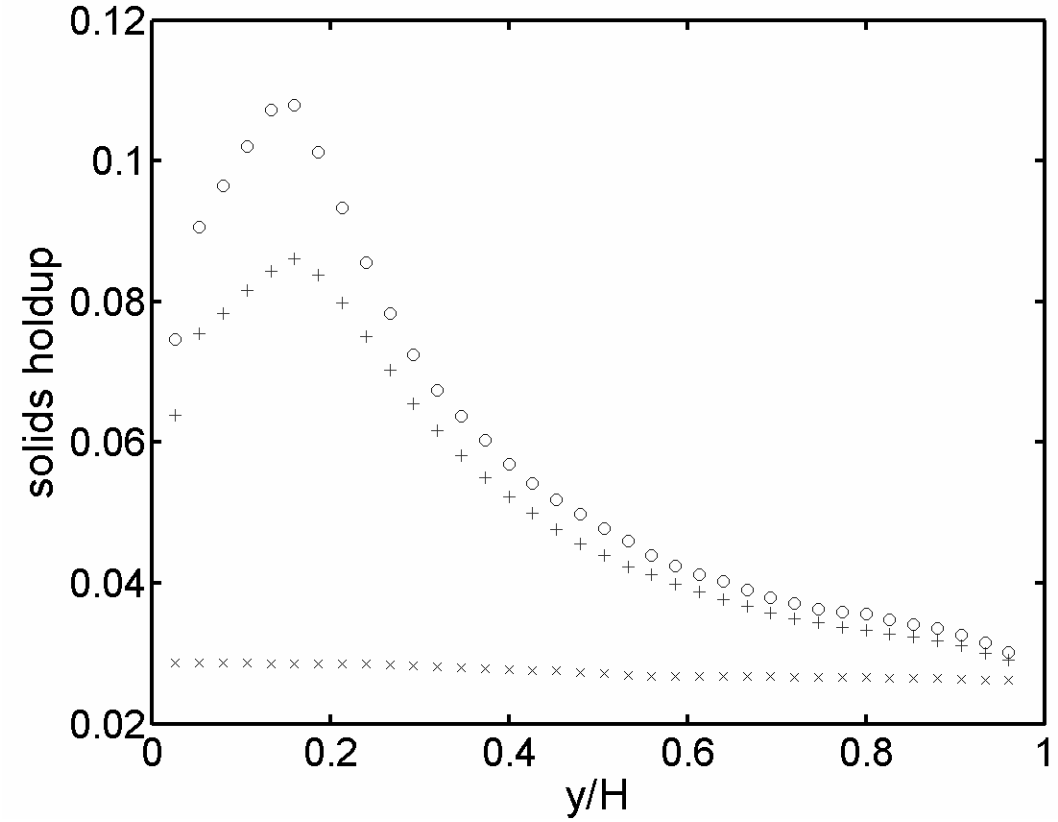

Figure 8: Axial variation of laterally averaged particle volume fraction corresponding to statistical steady state. Results obtained from coarse-grid simulations with stochastic (+) and time-averaged (o) sub-grid models are compared. Also shown as (x) are results corresponding to kinetic theory (i.e. with no sub-grid models). No slip boundary conditions. Uniform inlet conditions. The riser geometry and conditions are the same as in figures 2 and 3.

peak at the intermediate elevation. It is clear from figure 8 that the time-averaged and stochastic sub-grid models lead to quantitatively different results near the inlet but converge at higher riser elevations. Figure 9 shows the lateral profiles of particle volume fraction and dimensionless particle flux at an elevation of 80% of the riser height, where the laterally averaged particle volume fractions obtained with the stochastic and time-averaged sub-grid models are fairly close. It is clear from this figure that both models

predict enrichment of particle concentration and downflow near the wall region. The results are quantitatively different, but the difference is not very large. Although we do not attempt any comparison with experimental data in this study, we suspect that the uncertainties in the experimental data will be at least as large as the differences between these two model predictions and that discrimination between these two models by comparison with experimental data in the upper elevation of risers is unlikely. On the other hand, discrimination may be possible at the lower elevations. However, the details of flow at the bottom are probably very sensitive to the spatial nonuniformities and fluctuations in the inlet flow (discussed later), and proper discrimination between models on the basis of experimental data will be difficult unless one carefully measures the inlet flow characteristics.

In any case, there is no doubt that the addition of a sub-grid model (be it the time-averaged sub-grid model or the stochastic sub-grid model) has dramatically altered the simulation results, establishing that results obtained by integrating the microscopic equations without any sub-grid correction are suspect.

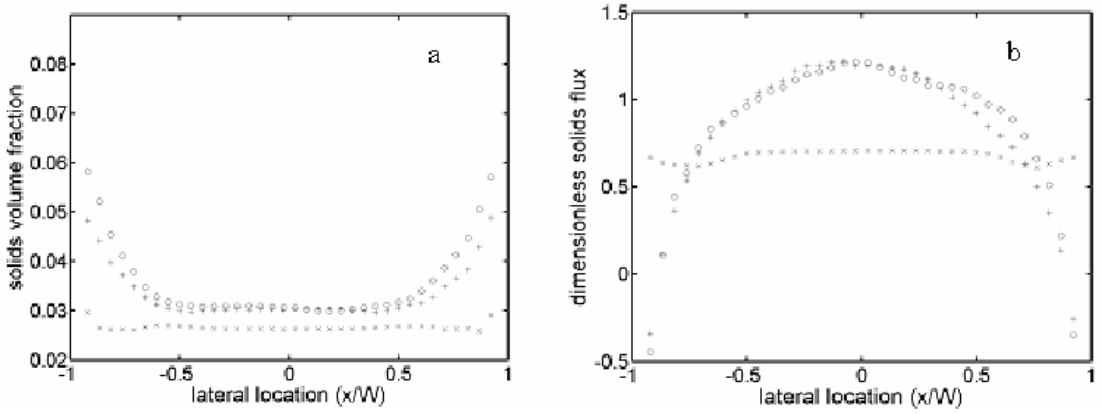

Figure 9: Lateral variations of (a) particle volume fraction and (b) dimensionless particle flux at an elevation of 80% of the riser height. Results obtained from coarse-grid simulations with stochastic (+) and time-averaged (o) sub-grid models are compared. Also shown as (x) are results corresponding to kinetic theory (i.e. with no sub-grid models). No slip boundary conditions. Uniform inlet conditions. The riser geometry and conditions are the same as in figures 2 and 3.

Coarse-grid simulations with free-slip boundary conditions

As discussed earlier, no-slip boundary condition at the solid walls (used in the simulations described above) is by no means accurate and a partial slip boundary condition (which is not too far from free slip) is probably more realistic. We explored the sensitivity of the coarse grid simulation results to the wall boundary conditions by repeating a number of simulations using free slip boundary conditions for both phases. Specifically, we started from a highly nonuniform initial state obtained via coarse grid simulation using the time-averaged or the stochastic sub-grid model and no-slip boundary conditions, and continued the simulation with free slip boundary conditions and desired sub-grid model. Once again, the fluctuations were washed out of the channel when no

sub-grid model was included. With the time-averaged and stochastic sub-grid models, fluctuations persisted. Figures 10a and 10b show snapshots of simulations with free slip boundary conditions; no dramatic, qualitative difference between the time-averaged and stochastic sub-grid models is apparent. Indeed, these snapshots are not much different from those obtained with no-slip boundary conditions, suggesting that the gross features of the fluctuating flow pattern in a statistical steady state are not driven by specific choice of wall boundary conditions.

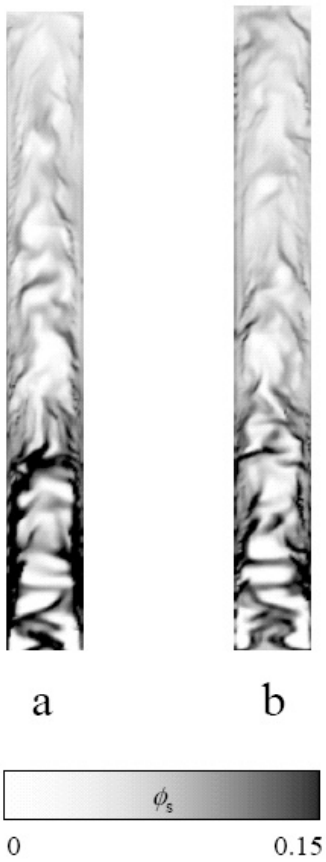

Figure 10: Snapshots of particle volume fractions obtained in the coarse-grid simulations. (a) Time-averaged sub-grid model, (b) stochastic sub-grid model. Free-slip boundary conditions for both phases.

Coarse grid simulations with free slip boundary conditions manifested sensitivity to the initial condition. When the above simulations were repeated, starting from an initially empty channel, nonuniform distribution of particles and persistent large-scale fluctuations in particle concentration did not develop with all three sub-grid models. This suggested that there are at least two attractors for simulations with free slip boundary conditions. Such a multiplicity has not been reported in any experimental study and is therefore likely to be unphysical. In practice, the inlet at the bottom is neither perfectly uniform nor steady, and spatial nonuniformities and temporal fluctuations are inevitable at the bottom inlet. Indeed, when we introduced stochastic, lateral variation in axial particle mass flux at the inlet to a simulation with stochastic sub-grid model, the nonuniform distribution of particles and persistent large-scale fluctuations readily developed even from a uniform initial condition (Andrews, 2003). Thus, nonuniformities or fluctuations at the inlet and/or some resistance at the solid walls to flow serve to eliminate spurious solutions.

Figure 11 presents the axial variation of laterally averaged particle volume fraction in the statistical steady state for simulations with free slip boundary conditions, a highly nonuniform initial condition, and uniform inlet. Once again, we see that the results obtained with the time-averaged and stochastic sub-grid models are qualitatively similar, while the result obtained in simulations with no sub-grid correction is grossly different. Comparison of figures 8 (no slip) and 11 (free slip) reveal no qualitative differences; however, the wall boundary conditions do seem to have a quantitative effect on the predicted holdup profile.

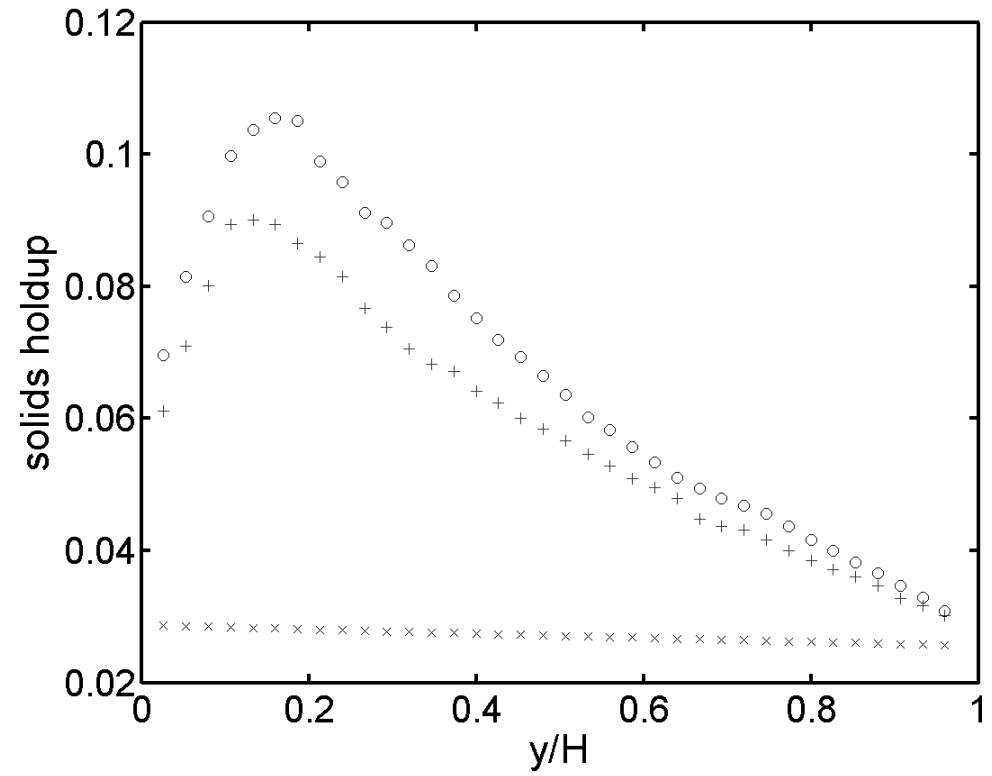

Figure 11: Axial variation of laterally averaged particle volume fraction corresponding to statistical steady state. Results obtained from coarse-grid simulations with stochastic (+) and time-averaged (o) sub-grid models are compared. Also shown as (x) are results corresponding to kinetic theory (i.e. with no sub-grid models). Free-slip boundary conditions. Uniform inlet conditions. The riser geometry and conditions are the same as in figures 2 and 3.

Figures 12a and 12b show lateral variation of particle volume fraction and dimensionless particle flux at an elevation of 80% of riser height. It is clear that the time-averaged and stochastic sub-grid models yield nearly the same results. Comparison of these figures with figures 9a and 9b reveals that a change in wall boundary conditions only contributes to a small quantitative change near the wall region.

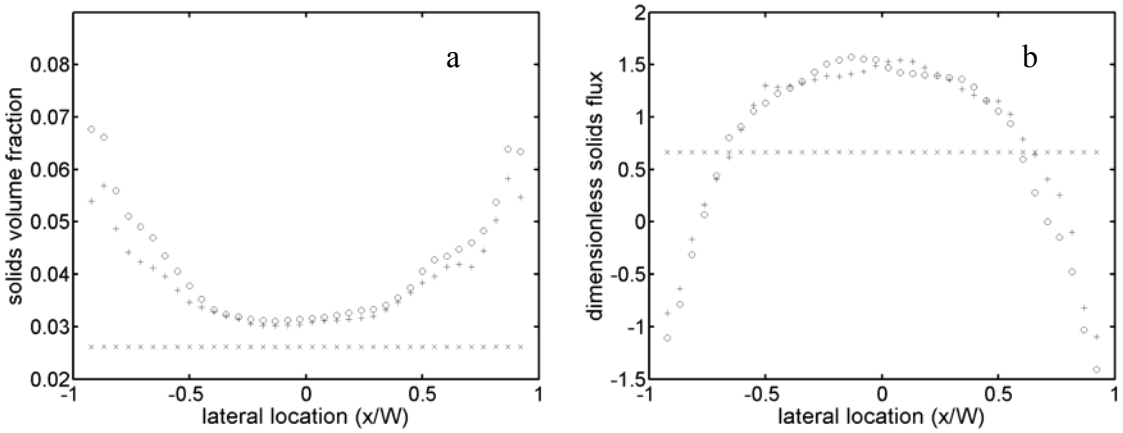

Figure 12: Lateral variations of (a) particle volume fraction and (b) dimensionless particle flux at an elevation of 80% of the riser height. Results obtained from coarse-grid simulations with stochastic (+) and time-averaged (o) sub-grid models are compared. Also shown as (x) are results corresponding to kinetic theory (i.e. with no sub-grid models). No slip boundary conditions. Uniform inlet conditions. The riser geometry and conditions are the same as in figures 2 and 3.

Discussion

Our simulations show clearly that the dominant fluctuations occurred at comparable dimensionless frequencies (which are much smaller than the inverse of dimensionless time step) in both coarse-grid and mesoscale calculations. This suggests that fluctuations derive from the same process at both scales. As fluctuations do occur in mesoscale simulations even in the absence of macroscale shear and in coarse-grid simulations with free-slip boundary conditions, we begin by examining instabilities associated with the governing equations of motion (without requiring an active role for the macroscale shear or exit configuration). In the absence of shear and exit effect, the governing equations support a simple solution where the gas-particle mixture travels up

the channel homogeneously with the slip velocity being adequate to support the weight of the particle – that is, the simplest version of riser flow is a vertically traveling homogeneous fluidized bed. It is well known that the dominant instability in homogeneously fluidized beds, as predicted by the averaged equations of motion with simple phenomenological closures where the particle phase pressure and viscosity are only functions of particle volume fraction, take the form of one-dimensional, vertically traveling wavefronts having no horizontal structure (Jackson, 2000). Two-dimensional linear stability analysis of a uniformly fluidized bed of infinite extent based on the microscopic (kinetic theory) equations used in the present study (Tan, 2000) revealed that the most unstable mode is an oblique wave, with the horizontal wavenumber being much smaller than the vertical wavenumber. Hence it is sufficient to focus our discussion on growth rates of vertically traveling wavefronts having no horizontal structure and the amplification of disturbances introduced at the bottom of the riser and convected upwards by the flow. The time available for amplification is comparable to the residence time of the mixture in the riser.

According to the microscopic (kinetic theory) equations, the homogeneously fluidized state is unstable to vertically traveling horizontal wavefronts whose wavelength is larger than a few particle diameters and the dominant mode has a wavelength of ten or so particle diameters. The growth rate of perturbations whose wavelength is much larger than that of the dominant mode is *much* smaller than that of the dominant mode. Thus, a homogeneously fluidized bed gives way to nonuniform structures in coarse-grid simulations much more slowly (provided it is not stabilized by numerical viscosity), than in highly resolved simulations. As a result, appreciable amplification of the initial

disturbances (which, in turn, can give way to lateral nonuniformities through secondary gravitational overturning instability, e.g., Batchelor, 1993; Glasser et al., 1996, 1997, 1998) does not occur in the coarse-grid simulations with free-slip boundaries within the time available in the riser flow and the disturbance gets washed out of the riser. Our observation that a highly nonuniform initial state (coupled with uniform inlet conditions) could not sustain the fluctuating state suggests that the basin of attraction for the homogeneous state is fairly large and/or that a fluctuating statistical steady state does not exist for the microscopic equations discretized on a coarse grid.

When modest stochastic, lateral variation was introduced in axial particle mass flux at the inlet, the fluctuations persisted in the riser (in our simulations of the microscopic equations discretized on a coarse grid coupled with free-slip boundary conditions); however, the time-averaged solution was only marginally different from that obtained without stochastic fluctuations, clearly suggesting that this solution was only a mild perturbation of the homogeneous solution.

Note that in our riser simulations the gas-particle mixture entered the riser in a plug flow manner. When no-slip boundary conditions are employed, both the fluid and the particles are forced to slow down near the wall and an increase in particle volume fraction must occur purely because of kinematic effect. This represents another form of lateral nonuniformity that can, in principle, develop into a fluctuating state. However, the particle phase viscosity in the homogeneous state is very small (when no sub-grid correction is included). Therefore, the boundary layer near the channel walls did not grow rapidly with distance from the inlet in our coarse-grid simulation examples (without any sub-grid correction) and the particle concentration near the channel walls did not grow

appreciably with height. Thus, lateral perturbation to the homogeneously fluidized state by the presence of the sidewalls was not large enough to give rise to and sustain the highly nonuniform fluctuating state.

Our computational experiments indicate that nonuniform solutions with sustained fluctuations and lateral segregations *may* develop in coarse-grid simulations of the microscopic equations only if pronounced nonuniformity is present at the inlet (such as side entrance, large scale fluctuations at the inlet, etc.).

Adding the time-averaged closure expressions in Table 3 to the microscopic model equations did *not* lead to an increase in the growth rate of perturbations to a homogeneously fluidized bed – if anything, the addition of a large mesoscale particle phase viscosity should decrease the growth rate! Thus, the difference in the outcome of the coarse-grid simulations with and without sub-grid models is *not* due to a larger growth rate of disturbances in the presence of sub-grid models. This is consistent with our observation that the fluctuating state could not be reached from uniform initial conditions (and uniform inlet conditions) when free slip boundary conditions were employed. The observation that the fluctuating state could be sustained if the simulations began with a nonuniform initial condition reveals coexistence of a homogeneous solution and a high-amplitude nonuniform solution. [Such coexistence of solutions for these equations have been demonstrated previously, see Glasser et al. (1996, 1997).] We found that adding stochastic, lateral fluctuations in particle mass flux at the inlet could eliminate the homogeneous state; thus, the homogeneous solution appears to have a small attractor basin. When no-slip boundary conditions are used in the simulations using sub-grid corrections, the boundary layer grows more rapidly than in the no sub-grid case, as the

particle phase viscosity is much larger when a sub-grid model is used. Consequently, particle accumulation near the wall region is more pronounced when a sub-grid model is used and this lateral nonuniformity is apparently enough to take the system into the basin of attraction for the fluctuating state.

Summary

It is clear from the examples presented here that the results obtained in coarse-grid integration of the microscopic equations for gas-particle flows in large process vessels can change appreciably if sub-grid corrections to account for the effects of unresolved structures are included. The most dramatic difference occurred in our simulations when a simple *time-averaged* sub-grid model was added to the *no sub-grid* model case. In view of this sensitivity, the results published in the literature where researchers have simply solved the continuum equations without corrections for sub-grid structures should be re-evaluated. Although the level of sophistication of the sub-grid model did make a difference in the quantitative results in our simulations, even a simple time-averaged sub-grid model appeared to capture the main qualitative effects.

The simple time-averaged sub-grid model is, in a strict sense, flawed, as there is no separation of time scales between the unresolved (sub-grid) structures and those resolved in the coarse-grid simulations. To account for this lack of separation of time scale, a rather simple enhancement of the time-averaged sub-grid model that took the form of a stochastic correction to the drag coefficient was implemented. It was found that such a stochastic sub-grid model yielded qualitatively the same results as the time-averaged sub-grid model. Thus the lack of separation of time scales does not appear to be a severe deficiency.

The approach employed in the present study to construct sub-grid models is clearly *ad hoc*. Such an approach is adequate, in our opinion, for our study as our primary goal is to expose the potential importance of sub-grid corrections. More in-depth study of the processes occurring at small scales is needed to develop meaningful and broadly useful sub-grid models.

It should also be emphasized that the present analysis only considered a static interphase interaction force – even though the stochastic part introduced a time-dependent character, it does not capture dynamic effects of the type examined by Zhang & VanderHeyden (2002), who argued that the mesoscale structures can lead to an appreciable added mass correction. Additional work is required to verify the existence of such a dynamic term – if it does exist, it may slow down the coarse-grid fluctuations appreciably and eliminate the need for a stochastic sub-grid model for the drag coefficient.

Acknowledgements

This work was supported by the US Department of Energy CDE-FC26-00NT40971.

References

Agrawal, K., Loezos, P. N., Syamlal, M. & Sundaresan, S., 2001 The Role of Meso-scale Structures in Rapid Gas-solid Flows. *J. Fluid Mech.*, **257**, 359 – 371.

Andrews, A. T., 2003 Unpublished results.

Batchelor, G. K., 1993 Secondary Instability of a Gas-Fluidized Bed. *J. Fluid Mech.*, **445**, 151 – 185

Benyahia, S., Arastoopour, H. & Knowlton, T. M., 2000 Simulation of particles and gas flow behavior in the riser section of a circulating fluidized bed using the kinetic theory approach for the particulate phase. *Powder Technol*., **112**, 24 – 33.

Benyahia, S., Arastoopour, H. & Knowlton, T. M., 2002 Two-dimensional transient numerical simulation of solids and gas flow in the riser section of a circulating fluidized bed. *Chem. Eng. Commun*., **189**, 510 –

Chang, H. & Louge, M., 1992 Fluid Dynamic Similarity of Circulating Fluidized-Beds. *Powder Technol.*, **70**, 259 – 270.

Deutsch, E. & Simonin, O., 1991 Turbulence modification in turbulent flow. ASME FED1991, **1**, 34 – 42.

Ding, J. & Gidaspow, D. 1990 A Bubbling Fluidization Model Using Kinetic-Theory of Granular Flow. *AIChE J*., 36, 523 – 538.

Enwald, H., Peirano, E., Almstedt, A. E. & Leckner, B., 1999 Simulation of the fluid dynamics of a bubbling fluidized bed. Experimental validation of the two-fluid model and evaluation of a parallel multiblock solver. *Chem. Eng. Sci.*, **54**, 311-328.

Enwald, H. & Almstedt, A. E., 1999 Fluid dynamics of a pressurized fluidized bed: comparison between numerical solutions from two-fluid models and experimental results. *Chem. Eng. Sci.*, **54**, 329-342.

Enwald, H., Peirano, E. & Almstedt, A. E., 1997 Eulerian two-phase theory applied to fluidization. *Int. J. Multiphase Flow* **22**, Suppl., 21-66.

Gelderbloom, S. J., Gidaspow, D. & Lyczkowski, R. W., 2003 CFD simulations of bubbling/collapsing fluidized beds for three Geldart groups. *AIChE J*., **49**, 844 – 858.

Gidaspow, D., 1994 *Multiphase Flow and Fluidization*, Academic Press, CA.

Glasser, B. J., Kevrekidis, I. G. & Sundaresan, S., 1996, One- and two-dimensional travelling wave solutions in gas-fluidized beds. *J. Fluid Mech*. **306**, 183 – 221.

Glasser, B. J., Kevrekidis, I. G. & Sundaresan, S., 1997 Fully developed travelling wave solutions and bubble formation in fluidized beds. *J. Fluid mech*. **334**, 157 – 188.

Glasser, B. J., Sundaresan, S. & Kevrekidis, I. G., 1998 From bubbles to clusters in fluidized beds. *Phys. Rev. Lett*., **81**, 1849 – 1852.

Goldschmidt, M. J. V., Kuipers, J. A. M. & van Swaaij, W. P. M., 2001 Hydrodynamic modeling of dense gas-fluidized beds using the kinetic theory of granular flow: Effect of restitution coefficient on bed dynamics. *Chem. Eng. Sci.*, **56**, 571 – 578.

Jackson, R., 2000 *The dynamics of fluidized particles*. Cambridge University Press.

Koch, D. L. & Sangani, A. S., 1999 Particle pressure and marginal stability limits for a homogeneous monodisperse gas fluidized bed: kinetic theory and numerical simulations. *J. Fluid Mech.*, *400*, 229 – 263.

Lu, H. L. & Gidaspow, D., 2003 Hydrodynamic simulations of gas-solid flow in a riser. *Ind. Eng. Chem. Res.*, 42, 2390 – 2398.

Lun, C. K. K., Savage, S. B., Jeffrey, D. J. & Chepurniy, N., 1984 Kinetic theories of granular flows: inelastic particles in Couette flow and slightly inelastic particles in a general flow field. *J. Fluid Mech.*, **140**, 223 – 256.

Neri, A. & Gidaspow, D., 2000 Riser hydrodynamics: Simulation using kinetic theory. *AIChE J*., **46**, 52 – 67.

Nieuwland, J. J., Annaland M. V., Kuipers, J. A. M. & van Swaaij, W. P. M., 1996 Hydrodynamic modelling of gas/particle flows in riser reactors. *AIChE J.*, **42**, 1569 – 1582.

Nieuwland, J. J., Huizenga, J. J. P., Kuipers, J. A. M. & van Swaaij, W. P. M., 1995 Hydrodynamic modelling of circulating fluidized beds. *Chem. Eng. Sci.*, **49**, 5803 – 5811.

Samuelsberg, A. & Hjertager, B. 1996 Computational modelling of gas/particle flow in a riser. *AIChE J.*, **42**, 1536 – 1546.

Sun, B. & Gidaspow, D., 1999 Computation of circulating fluidized bed riser flow for the Fluidization VIII benchmark test. *Ind. Eng. Chem. Res.*, **38**, 787 – 792.

Sundaresan, S., 2000 Perspective: Modeling the Hydrodynamics of Multiphase Flow Reactors: Current Status and Challenges. *AIChE J.*, **46**, 1102 – 1105.

Syamlal, M. December 1998 MFIX Documentation: Numerical Techniques. DOE/MC-31346-5824. NTIS/DE98002029.

Syamlal, M., Rogers, W. & O'Brien, T. J., 1993 MFIX Documentation, U.S. Department of Energy, Federal Energy Technology Center, Morgantown.

Tan, J., 2000 2 – D stability analysis of gas-particle flows in risers, BSE Thesis, Department of Chemical Engineering, Princeton University, Princeton, New Jersey, USA.

Tsuo, Y. P. & Gidaspow, D., 1990 Computation of flow patterns in circulating fluidized beds. *AIChE J.*, **36**, 885 – 896.

Uhlenbeck, G. E. & Ornstein, L. S., 1930 On the theory of Brownian motion. *Phys Rev.*, **36**, 823 – 841.

Van Wachem, B. G. M., Schouten, J. C., van den Bleek, C. M., Krishna, R. & Sinclair, J. L., 2001 Comaparative analysis of CFD models of dense gas-solid systems. *AIChE J.*, **47**, 1035 – 1051.

Wen, C. Y. & Yu, Y. H., 1966 Mechanics of Fluidization. *Chem. Eng. Prog. Symp. Ser.*, **62**, 100 – 111.

Zhang, D. Z. & VanderHeyden, W. B., 2001 High-resolution three-dimensional numerical simulation of a circulating fluidized bed. *Powder Technol.*, **116**, 133 – 141.

Zhang, D. Z. & VanderHeyden, W. B., 2002 The effects of mesoscale structures on the macroscopic momentum equations for two-phase flows. *Int. J. Multiphase Flow*, **28**, 805 – 822.

Appendix A

Eqs. (1) – (4) describe the continuity and momentum balance equations for the particle and gas phases. Here, ϕ is the volume fraction of particles; $\underline{v}$ and $\underline{u}$ are the local average velocities of the particle and gas phases, respectively; ρ_s and ρ_g are the densities; $\underline{\underline{\sigma}}_s$ and $\underline{\underline{\sigma}}_g$ are the stress tensors associated with the two phases expressed in a compressive sense; $\underline{f}$ is the interaction force between the phases per unit volume of the bed; and $\underline{g}$ is the specific gravity force. Eq. (5) is the pseudothermal energy (PTE) balance, where T is the granular temperature – in this equation, $\underline{q}$ is the diffusive flux of PTE; the second and third terms on the right hand side quantify the rates of production of PTE by shear and gas-particle slip, respectively. The fourth and the fifth terms account for the rates of dissipation of PTE through inelastic collisions and viscous damping, respectively.

Eq. (6) describes a simple Newtonian closure for the effective gas phase stress. Here p_g and $\hat{\mu}_g$ denote fluid phase pressure and effective viscosity, respectively. In the regime investigated in the present study, namely, $\rho_s\phi >> \rho_g(1-\phi)$, the contribution due to the deviatoric part of the gas phase stress is negligible.

The gas-particle interaction force, $\underline{f}$, is, for all practical purposes, only due to drag. Eq. (7) describes the drag correlation used in our simulations (Wen and Yu, 1966). Here β, C_D, d, μ_g and Re_g denote an effective drag coefficient for the suspension, single particle drag coefficient, particle diameter, fluid viscosity and Reynolds number, respectively.

Eq. (8) summarizes a kinetic theory closure for the particle phase stress in the fluid-particle mixture. An expanded discussion of this closure can be found in Agrawal et al. (2001). Here e_p denotes the coefficient of restitution for particle-particle collisions, and the spheres are assumed to be smooth. Eq. (9) is the corresponding closure for the diffusive flux of PTE.

Eq. (10) is the kinetic theory closure for the rate of dissipation of PTE through inelastic collisions, while eq. (11) represents the closure due to Koch & Sangani (1999) for the rate of dissipation of PTE by viscous dissipation in the fluid phase.

Silo Music and Silo Quake: Granular Flow Induced Vibration

Benson K. Muite, Shandon F. Quinn and Sankaran Sundaresan*
School of Engineering and Applied Science,
Princeton University,
Princeton, NJ 08544, USA

And

K. Kesava Rao
Department of Chemical Engineering,
Indian Institute of Science,
Bangalore, India

Keywords: Silo quake, silo music, stick-slip flow, resonance, creep, granular discharge

Submitted to Powder Technology
September 2003

*Corresponding author. Tel.: +1-609-258-4583; fax: +1-609-258-0211

E-mail address: sundar@princeton.edu (S. Sundaresan)

Abstract

Acceleration and sound measurements during granular discharge from silos are used to show that silo music is a sound resonance produced by silo quake. The latter is produced by stick-slip friction between the wall and the granular material in tall narrow silos. For the discharge rates studied, the occurrence and frequency of flow pulsations are determined primarily by the surface properties of the granular material and the silo wall. The measurements show that the pulsating motion of the granular material drives the oscillatory motion of the silo and the occurrence of silo quake does not require a resonant interaction between the silo and the granular material.

1 Introduction

The discharge of granular materials from silos is often characterized by vibrations or pulsations of the silo, termed 'silo quake', and a loud noise, termed 'silo music' [1-8]. Both of these are undesirable as silo quake may cause structural failure and silo music is a source of noise pollution. Unfortunately, the numerous conflicting studies published in the literature [1-8] do not give the silo designer a simple model to understand the physical processes that cause the pulsations, and to guide silo design or modification that would prevent the pulsations or at least minimize their effect. The purpose of this study is to investigate the cause of the noise and the pulsations, and the interaction between the motion of the granular material and the motion of the structure.

Several studies of the discharge of granular material from silos have noted fluctuations in discharge rate and the production of noise and vibration [1-8]. The top of the granular material has been observed to move in discrete steps even though the discharge from the bottom of the silo was continuous [4,6]. For smooth-walled, tall, narrow silos, pulsations occurred during both mass and mixed flow. The pulsations were observed to stop at a critical height of granular material in the silo [1,3]. Methods suggested for preventing pulsations include roughening the walls in the transition zone between the bunker and the orifice [1-3] and placement of inserts along the silo walls [4].

In an early study, Phillips [6] observed the motion of sand in a tube, which had a glass face, and was closed at the lower end by a flat bottom having a central orifice. When the orifice was opened, the sand in the upper part of the tube moved downward intermittently in jerks. Phillips noted, "when the flow begins, a curious rattling sound is heard which changes to a distinct musical note". He also did experiments in which the tube was first partly filled with mercury and then filled with sand. Once again, the free surface of the sand descended intermittently when the mercury was allowed to flow through the orifice. He observed that the length of the column of sand increased by about 2% during the 'stick' phase. Further, the motion of the granular material caused the wall of the tube to vibrate. Thus both silo music and silo quake occurred in his experiments, and he suggested that the stick-slip motion of the sand may be responsible for these phenomena.

Some recent studies have suggested that the pulsations are due to a resonant interaction between the granular material and the silo structure [1,7]. Unfortunately, these studies have been done in complicated systems where it is difficult to uncouple the effects of the vibrating structure from the pulsation of the granular material. In particular, understanding the source of measured tube wall vibration frequencies without a good numerical or theoretical model is difficult [9]. Further, a study has been conducted where the measured natural frequency of free vertical oscillation of the structure was

significantly larger than the pulsation frequency, suggesting resonance did not occur [4]. Tejchman [1] also noted that the magnitude and presence of the flow pulsations was influenced by environmental factors such as temperature and electrostatic effects, which suggests that resonant interaction may not be required for pulsations to occur.

Wensrich [5] has proposed that these pulsations are due to compression and dilation waves in the granular material, which are created by stick-slip motion between the granular material and the silo walls. He found that at the very low discharge rates examined in his study (corresponding to average particle velocities in the cylindrical tube of 0.4 mm/s or smaller), the pulsation frequency was inversely proportional to the discharge rate. Pulsations have also been observed in funnel flow bunkers, where the granular material at the walls does not slip during discharge [4]. Wensrich [5] has suggested that the pulsation creation mechanism is entirely different in funnel flow, but does not give evidence to support his conjecture.

Hardow et al. [4] have suggested that the pulsations are due to the rapid acceleration and deceleration of the granular material in the bin section, caused by the stress fluctuations in the granular material in the hopper section. As the granular material in the hopper region deforms, there are periods where the mass of granular material in the bin is not supported and collapses in a downward step creating a large impulse, which shakes the silo structure. This study observed pulsations during core flow in a silo that was 6 m high, 0.6 m deep and 1.2 m wide, and hence the flow kinematics were considerably different from those in tall narrow silos.

Finally, Moriyama and Jimbo's [2] findings suggest that the magnitude of the pulsations is determined by how the granular material changes from a compressed state in the bunker to a dilated state in the hopper. Moriyama and Jimbo [2] also found that the likelihood a silo will discharge with pulsations is dependent on the method used to fill the silo. They did not propose a physical mechanism to explain their observations.

The aim of the present study, which is largely experimental, is to obtain a mechanistic understanding of silo music and flow pulsations. Through a combination of sound, bed height, and acceleration measurements, it is shown that silo music is driven by the stick-slip pulsating motion of the granular material during discharge and is associated with a sound resonance in the air column above the bed. Since previous studies have suggested a resonant interaction between the granular flow and silo structure as the possible cause for the pulsating motion of the granular material [1,7], a model silo system having a single dominant natural (vibration) frequency for vertical oscillations, which can be varied systematically was designed for this study. This has allowed a study of the interaction between the granular flow and the silo structure, which conclusively demonstrates that a resonant interaction between the granular material and the silo structure is not required to establish pulsating flow and silo music. Different wall and granular materials have been used to probe their role on flow pulsations and silo music during silo discharge.

2 Experimental Method

In this section, a description of (a) the model silo used in the study, which behaves like an oscillator with a single degree of freedom, (b) the properties of the granular and silo materials, (c) the characteristics of the accelerometers used to measure the motion of the silo and the granular material, and (d) the procedure used to obtain the sound measurements are provided.

Aluminum, steel, and acrylic tubes, open at the top and covered at the bottom with a flat acrylic plate having a concentric orifice (see below for details of this plate), were used as silos. A number of experiments were conducted using silos resting on supporting springs (see figure 1), which in turn were attached to a steel frame that was rigidly connected to the laboratory walls. The silo was also equipped with rollers and sliders, which were attached to the steel frame. These allowed vertical oscillation of the silos and restricted lateral motion. The supporting springs had spring constants ranging from 4 to 2265 N/mm. Experiments were also done using an aluminum block in place of the spring, or simply bolting the silo directly to the supporting steel frame – these configurations afforded the two largest natural frequencies for vertical silo oscillation reported in this study. Properties of the tube and granular materials are listed in tables 1 and 2, respectively. Photographs of the granular materials, obtained using a microscope, are shown in figures 2, 3 and 4. The granular materials did not exhibit squeaking or booming when sheared. The temperature and humidity were recorded in each experiment. The temperature varied between 20˚C and 25˚C (from one day to another), and the relative humidity between 18 and 40%. During experiments with each tube and granular material combination (which lasted a few hours) the humidity variation was within 5% and the temperature variation was within 2˚C.

Since structural accelerations were measured, care was taken to ensure that the apparatus had a single controlled dominant natural frequency for vertical oscillations. The natural frequency of vertical oscillations was changed by using different springs between the silo and the steel frame. In these experiments, the metal tubes were chosen to have large natural frequencies, so that when the structure was excited by a broadband impulse in the vertical direction, the dominant natural frequency was due to the mass-spring system, and not the intrinsic vibration of the tube. For further details, see Muite [10]. The acrylic tube had a natural frequency of 350 Hz, which while not as large as the metal tubes was still several times greater than the pulsation and lowest structural natural frequencies.

Acrylic plates with centrally located orifices (with diameters between 13 and 25 mm) were bolted to a 1.21 Kg aluminum flange, which was screwed on the bottom of the tubes. To fill the silo, the orifice at the bottom of the tube was first sealed with a piece of duct tape. The granular material was poured into the silo through a funnel placed at the top of the tube. Stripping away the duct tape seal over the orifice initiated discharge. The mean discharge rate was measured using a stopwatch. For the acrylic tube, the height of material in the silo could also be measured during discharge to confirm that the discharge rate was constant with time. To ensure that the tubes had reached a steady state of wear, the granular material was discharged several times through the same tube before final measurements were taken. Steady state wear was reached when repeatable granular material acceleration measurements could be taken.

Accelerations were measured both in the granular material and on the silo structure. Vertical accelerations inside the granular material were measured using a unidirectional Kistler 8774A50 low-impedance ceramic shear accelerometer with an output sensitivity that deviated less than 1.5 % for frequencies between 10 Hz and 10 KHz. The accelerometer was embedded approximately 50 mm below the top surface of the granular material. This depth ensured that during discharge the accelerometer was held upright by the granular material and was still shallow enough that the acceleration could be measured for the bulk of the discharge. As the granular material discharged, the accelerometer cable was carefully fed into the silo to ensure that the cable did not affect the motion of the accelerometer. This accelerometer had a range of $\pm$ 500 m/s^2 and was accurate to within $\pm$ 5 m/s^2. It had a diameter of 8 mm, a length of 26 mm, and a mass of 4 g, and so was considerably larger than a

sand grain. However, the wide frequency response allowed better time resolution of the bulk granular material acceleration than would be possible with smaller accelerometers of comparable cost.

Silo structural vibrations were measured using a Kistler 8784A5 low-impedance ceramic shear accelerometer which has a greater sensitivity but a smaller range than the accelerometer used to measure granular material accelerations. To measure vertical accelerations, this accelerometer was wax mounted on the flange at the bottom of the silo. This accelerometer had a sensitivity that varied by less than 0.5 % for frequencies between 10 Hz and 6 KHz. It had a range up to $\pm$ 50 m/s^2, an accuracy of $\pm$ 0.5 m/s^2, and a mass of 21 g.

The accelerometer output was sent through a Kistler 5118B2 signal conditioner to a Measurement Computing PCI-DAS1002 data acquisition card on a 400 MHz Pentium II computer. The sampling rate on the data acquisition card was 20 KHz. For both accelerometers, the manufacturer supplied calibration was used to convert the accelerometer voltage output to acceleration. The accelerometers could not be used simultaneously since only one data acquisition system was available.

The bulk of the sound measurements were made in an apparatus made from an acrylic tube for which the resonant frequency of the structure was not well controlled [11]. However, several measurements were then repeated in the experimental setup used for the acceleration measurements to check that the same results were obtained. In these experiments an omnidirectional Optimus 33-3026 lapel microphone with a constant amplitude response for a frequency range between 30 Hz and 15 KHz was used to collect the sound data through a sound card on a personal computer. During discharge, the sound was recorded and a discrete Fourier transform of one second of sound data was used to determine the dominant frequency as a function of time during discharge. In the acrylic tube, the time at which the top of the granular material crossed a marked height in the tube during discharge was also recorded using a stopwatch. From these measurements the height of the granular material as a function of time since discharge started was found.

3 Results

To present the trends that are useful in determining the pulsation mechanism, sound measurements are only presented for sand discharging from the acrylic tube and acceleration measurements are shown primarily for crushed glass particles discharging from the aluminum and acrylic tubes. Measurements for glass beads are also presented. For more measurements of silo music produced by sand discharging from an acrylic tube see Quinn [11] and for more acceleration measurements during granular flow pulsations see Muite [10]. The variation of the pulsation frequency with the natural frequency of vertical oscillations of the silo is examined for all tube and granular material combinations, except for the plain steel tube, as pulsations did not occur in this tube. Silo pulsations also did not occur when sand was discharged from the aluminum tube, but did occur when sand was discharged from the acrylic and galvanized steel tubes.

3.1 Sound measurements

Figure 5 shows the sound intensity level as a function of time for discharge of sand from the acrylic tube. The discharge lasted for 51 s and as shown in the figure, silo music occurred for

approximately half of this time. Figure 6 shows a typical power spectrum for the sound measurements during discharge (determined by analyzing data obtained over a 1 s time interval). There are three types of prominent peaks. The first peak is at a frequency of approximately 40 Hz and it will be shown later that this is the pulsation frequency of the granular material and silo combination. The second peak corresponds to the resonant frequency for the air column above the tube (this resonance is well documented and a good account can be found in Rayleigh [12]). At the time the data shown in the figure was collected, this frequency was 200 Hz. The fact that this peak represents a resonance frequency is demonstrated in Figure 7, which shows the quarter wavelength corresponding to this frequency as a function of time since the beginning of discharge. The wavelength, λ, is found from the relationship $\lambda=c/f_a$ where c is the speed of sound in air and f_a is the frequency. Also shown is the height of the air column above the sand in the tube. This figure shows that the dominant quarter wavelength and the height of the air column are the same confirming the resonant behavior. It is clear from the *quarter* wavelength, that this resonance corresponds to a standing wave mode with a node at the granular material surface, and an anti-node at the open end of the tube (as the open end of the tube cannot be a node). Figure 6 also shows a number of other peaks at higher frequencies, which are simply the odd harmonics of the fundamental (lowest) resonance frequency of the air column.

3.2 Determination of the natural frequency for vertical oscillations of the silo

Figure 8 shows a typical measurement to determine the natural frequency of vertical silo oscillations. In these measurements, the silo was filled with granular material and the orifice closed. The base of the filled silo was then struck with a soft mallet and the resulting acceleration during free oscillations recorded. The dominant natural frequency of the silo structure was found either by using the largest peak in the power spectrum of the acceleration, or by counting the number of free oscillations during a specified time directly from the acceleration measurements. The two measurements gave essentially the same results; however, when the natural frequency was less than 30 Hz, counting the number of oscillations in a specified time gave a more accurate measurement of the natural frequency than locating the center of the broad peak obtained from the power spectrum. Similarly when the natural frequency was large, the power spectrum was a better indicator of the natural frequency because an unambiguous sharp peak could be located, while the acceleration vs. time trace showed rapidly decaying oscillations which were not easy to count. For spring constants, $k < 1000$ N/mm, the observed natural frequency was approximately equal to $f_n = (1/2\pi)(k/m)^{1/2}$, where m is the oscillating mass and f_n is the theoretical natural frequency for a spring mass system. For $k > 1000$ N/mm, the natural frequency of vertical silo motions was significantly less than f_n, possibly because of flange deformations, which reduced the effective stiffness of the system. This effect was important for natural frequencies greater than 25 Hz.

3.3 Acceleration measurements during discharge

Figure 9 shows measurements of the vertical acceleration of the silo when crushed glass was discharged through a 1.9 cm orifice. The accelerometer was mounted on the base of the silo. Once flow started, there was a period of pulsations during which the silo experienced large negative accelerations towards the earth. Half way during the pulsations, the magnitude of the negative pulsations suddenly doubled. After the granular material fell below a critical level, the pulsations stopped, and the silo structure experienced only small accelerations until the flow ended. While the pulsations occurred

regularly, this doubling of the pulsation magnitude was not always repeatable. It is not clear what changes in the flow resulted in these changes in the magnitude of the pulsations since the basic setup was unchanged from run to run.

The close up of the acceleration measured during pulsations shown in figure 10 reveals that the periods of large negative accelerations were short compared to the gradual rebound after each pulsation. Over this time scale, the pulsations had a very reproducible and steady frequency, but the absolute magnitude of the maximum acceleration varied from pulse to pulse.

Figure 11a shows measurements obtained with the accelerometer buried in the granular material. The flow conditions were the same as in figure 9, except that the orifice diameter was 1.3 cm instead of 1.9 cm. Also as in figure 9, negative accelerations are to the earth. Figure 11a shows that large positive accelerations occurred in the granular material during pulsations, while figure 9 shows that the silo experienced large negative accelerations. The two figures show that during each pulsation, the granular material fell a short distance and impacted the tube wall and flange bottom.

The close-up of the pulsations in figure 12a shows that despite the difference in flow rate, the pulsation frequency of 30 Hz is the same for discharge of granular material through a 1.3 cm orifice (figure 10) and through a 1.9 cm orifice (figure 12a). Figures 10 and 12a also show that the pulsation frequency in the granular material is the same frequency with which the silo moves, suggesting that the motion of the granular material drives the motion of the silo. Figure 12a also shows that each pulsation was followed by a negative acceleration within the material and then a second large positive acceleration, after which the acceleration of the granular material was close to zero until the next pulsation. Figure 13a shows a power spectrum for the acceleration measured during 1 second of pulsations in the crushed glass. It has a peak at the pulsation frequency of 30 Hz followed by a flat band region between 200 and 1000 Hz after which the power spectrum decays.

Figures 11b, 12b, and 13b are similar to figures 11a, 12a and 13a, but are for glass beads discharging through a 1.9 cm orifice from a silo resting on a 22 N/mm spring. The pulsations again stop at a critical height and the individual pulsations can be seen in figure 11b. The nature of each pulsation for glass beads (figure 12b) is a little different than for the crushed glass (figure 12a) and this is reflected in their power spectra, (figures 13a and 13b). Both spectra have the same high frequency decay for frequencies above 1000 Hz; however, for frequencies below 1000 Hz the glass beads have a larger number of distinct harmonics than the crushed glass. The crushed glass power spectrum is typical of white noise with a high frequency cutoff, while the glass bead power spectrum is typical of a signal produced by a well correlated periodic, but non-sinusoidal function [13].

In figures 10, 12a, and 12b the maximum downward accelerations of the silo and particles are roughly comparable, whereas the maximum upward acceleration of the granular material is significantly greater than that of the silo. This suggests that during each pulsation, the granular material slips past the silo walls and is forced to rest over a very short time period. This impact creates a shock wave which travels through the granular material and is recorded as the large upward acceleration. The granular material and silo then move together so that the resulting accelerations are of similar magnitude.

3.4 Dependence of the pulsation frequency of the granular material on the natural frequency of vertical silo vibrations

Figures 14, 15, and 16 show the variation of the pulsation frequency of the granular material for different granular material and silo wall combinations, as a function of the natural frequency of vertical oscillations of the silo. The pulsation frequency was determined in two ways. First, by counting peaks above a threshold value when the accelerometer was placed in the granular material and second by finding the largest component in the power spectrum when acceleration was measured on the base of the silo. These two methods were used because the power spectrum for acceleration in the granular material gave many harmonics and the lowest frequency did not always have the largest power. Similarly counting silo oscillations was not as precise as locating the single sharp peak in the power spectrum. However, in most cases, the results from the two methods were comparable. The pulsation frequency was determined for each second of flow pulsations and an average pulsation frequency during pulsating discharge obtained. The standard deviation in the average frequency measured during a single discharge was typically less than 10%.

When the silo had a free oscillation frequency below 25 Hz, the pulsation frequency had no dependence on the natural frequency of the silo as shown in figures 14, 15, and 16. Figure 15 also shows that doubling the orifice diameter and hence increasing the discharge rate by a factor of 6 had a negligible effect on the pulsation frequency (doubling the orifice diameter gives a six-fold increase in discharge rate in a silo of constant cross sectional area, because the discharge rate is proportional to the orifice diameter to the power 2.5, see Nedderman [14] for more details). The pulsation frequency was solely determined by the silo wall and granular material properties. For silo free oscillation frequencies above 25 Hz, the pulsation frequency had a positive correlation with the free oscillation frequency for all granular material tube wall combinations that pulsated, except for the acrylic and crushed glass combination. These figures show that the pulsations were not due to a resonant interaction with the silo structure, even though the motion of the silo can couple with the motion of the granular material and influence the frequency of pulsations. The three figures show that glass beads have similar frequency behavior in the acrylic and aluminum silos, but they have a higher pulsation frequency in the galvanized steel silo. Crushed glass has a lower pulsation frequency in the aluminum silo as compared to the acrylic silo, and a higher pulsation frequency in the galvanized steel silo compared to the acrylic silo. Since sand did not pulsate during discharge from the aluminum silo, no data points are shown.

3.5 Critical Height

The critical height is taken as the height of the granular material above the base of the silo at which pulsations stop. The time at which this occurred was recorded from the acceleration measurements, and as the discharge rate was independent of time, the critical height could be calculated. This method gave critical heights that were in agreement with direct measurements made for the transparent acrylic silo. The critical height did not vary by more than 0.1 m when the orifice diameter and spring constant were changed as long as the resonance frequency of vertical oscillations of the filled tube was less than 25 Hz. For frequencies above this, the variation of critical height with silo and granular material properties was not closely examined.

For all the granular materials, the critical heights for the acrylic silo were smaller than those for the aluminum and galvanized steel silos (table 3). In the aluminum silo, crushed glass had a significantly smaller critical height than glass beads. In both the galvanized steel and acrylic silos, all three granular materials had similar critical heights.

In the aluminum silo, an experiment was performed where the top of the granular material was loaded with a known weight after the silo had been filled. The weights were placed on top of the center of the granular material in the filled silo and did not touch the walls of the silo. The critical height and pulsation frequency were measured using time and acceleration measurements during discharge. The pulsation frequency was independent of the overload. As shown in figure 17, the critical height for glass beads was insensitive to the imposed overload, whereas that for crushed glass decreased linearly with the imposed overload. Experiments in the acrylic silo gave similar results.

4 Discussion

The goals of this study were to investigate the basic mechanism that causes silo music and silo quake, and to understand the interaction between the silo structure and the granular material during silo quake. In this section, a summary of the experimental results is given and a mechanism for the production of the pulsations is suggested. The results are then compared with those obtained in previous work on pulsating granular materials and some suggestions for further work are made.

The main observations of this investigation are:

1) In tall, narrow silos, silo quake is due to the frictional interaction between the granular material and the silo walls.
2) Silo music is created by silo quake and is a quarter wave sound resonance in the air column above the granular material.
3) Silo quake can occur without silo structural resonance.
4) A stick-slip regime has been observed where the motion of the granular material drives the motion of the silo. In this regime, the pulsation frequency has a narrow band distribution and does not depend on the discharge rate.
5) The upward acceleration of the granular material can reach up to 500 m/s^2, while the maximum acceleration of the silo was observed to be less than 15 m/s^2.

Before discussing pulsating flow, it is worth reviewing the generally understood kinematics of the discharge of granular material from a bin or hopper. Experiments show that in a tall, flat-bottomed cylindrical bin, with walls having a lower friction coefficient than the internal friction angle of the granular material, there is a region of plug flow at the top of the full silo. As the silo empties, the size of the plug flow region decreases and eventually all of the flowing material is in converging flow. The discharge rate from the bin is independent of the height of material in the bin, provided the height is greater than a few multiples of the diameter of the silo [20] and scales as $g^{1/2}D^{5/2}$, where D is the orifice diameter.

Radiographic studies of slow dense granular flow in model bunkers show that velocity discontinuities exist at the transition from the bin to the hopper [15]. Measurements in a discharging

bunker indicate that there exists a dynamic arch at the transition where the nature of the material flow changes from one without deformation (above the arch) to one where material deforms (below the arch) as it approaches the orifice [16]. Pressure measurements [2,4,7] near the transition from the bin to the hopper indicate that there is also a stress discontinuity [16] and that there are large pulsating stresses, which correspond to the cyclical formation and breakage of the dynamic arch. This pulsating behavior only occurs for dense assemblies [16,17].

These experiments were done in a flat bottomed silo, whereas the experiments that identified the dynamic arch [16] were conducted in a bunker where the bin to hopper transition determined the location of the dynamic arch. In the silo used in this study, the stagnant material adjacent to the orifice creates a hopper-like region. So the discharge from a flat bottomed silo may be expected to show many of the features observed in bunkers. If the density of the material in the plug flow region above the dynamic arch is high, it must dilate as it crosses the arch in order to deform in the hopper-like region.

Stick-slip motion in granular materials has also been studied in geometries other than silos. Nasuno et al. [18] performed simple shear tests with 70 - 110 μm glass beads and 100 - 600 μm sand. They observed stick-slip motion at low slip rates, which became continuous at very large slip rates. They also observed that at very small driving velocities, the period of fluctuations was inversely proportional to the driving velocity. For glass beads, the system fluctuated with near constant period, while for sand, the period varied stochastically. As the sliding velocity was increased, the period became independent of velocity, and finally at large sliding velocities, the motion became continuous. In the simple shear experiments done by Nasuno et al. [18], the spring constant connecting the driving piston to the sliding mass was varied. The spring constant influenced both the pulsation frequency and the critical driving velocity at which the pulsation frequency became independent of the driving velocity.

Nasuno et al. [18] also observed that a lengthy period of slow vertical dilation preceded rapid slip events in the horizontal direction. This dilation was carefully measured by Geminard et al. [19]. Their experiments suggest that in the shear zone particles climb slowly over each other. Once the particle is approximately 5% of a particle diameter over the particle below it, slip occurs and the top layer jumps forward before slowing down again and settling into another zone of particles [19]. In the experiments of Geminard et al. [19], the particle volume fraction was indistinguishable from the random close packed volume fraction of 63%.

These studies show that granular materials can undergo stick-slip motion, and that this can couple with the mechanical system (for example, a mass-spring system) in a complicated fashion, which depends on the system parameters. Together these studies suggest that stick-slip motion can occur in tall flat-bottomed silos during the discharge of granular materials. This leads to cyclical dynamic arch formation and breakage, which creates impulses that drive the silo structure. The stick-slip motion of the granular material can couple with the motion of the silo, but as shown by the results, the frequency of the stick-slip motion of the granular material need not be the same as the dominant natural frequency of the silo.

Armed with this background, one can compare the experimental observations in this study with those in previous studies to qualitatively explain the frequency dependence and the physical mechanism of stick-slip motion. As mentioned above, if the density of the material in the plug flow region above the arch is high, it must dilate as it crosses the arch in order to deform after it has passed the dynamic

arch. This dilation process and stick-slip friction in the granular material or at the silo wall can create granular material pulsations which originate at the arch. Excellent reviews on stick-slip friction can be found in Bowden and Tabor [21], Krim [22] and Berman et al. [23], who discuss the various postulated stick-slip friction mechanisms. The mechanism of most relevance to the present study is adhesive stick-slip friction which occurs when there are slowly weakening, time-dependent forces between the sliding surfaces. The forces are due to interactions at the contacts between the sliding surfaces which weaken after a typical lifetime.

The dynamic arch is a force chain – that is, a fragile network through which stresses are transmitted [24]. This arch supports a large fraction of the pressure above it and transmits this force to the walls of the silo. The arch is fragile, and consequently when the material below it has discharged enough so that the arch is unsupported from below, the slow creep typically observed in adhesive stick-slip begins. After the critical creep time during which the surface forces weaken, complete slip occurs collapsing the arch and creating a new arch. The process then repeats, giving rise to periodic impulses as the granular material above the arch moves in steps. During pulsations, material above the arch does not move smoothly, however material at the orifice exits continuously. This is the pulsation process observed in the present study, where the discharge rate is fast enough that it does not affect the pulsation frequency unlike in Wensrichs' study [5].

In Wensrichs' experiments [5], the entire bottom of a cylindrical model silo was slowly lowered. There is no region of converging flow, but there is a region near the bottom where the granular material dilates as the piston descends. Here the arch may be regarded as the boundary between the dense and dilated material.

For the *slow* discharge rates examined by Wensrich [5] where the average velocity of descent through the tube was 0.4 mm/s or smaller, creep was not the pulsation frequency determining step, and the arch collapsed whenever the particles below the arch had dropped enough to lose contact with the arch. Consequently, it is entirely reasonable that the pulsation frequency was inversely proportional to the discharge velocity. Wensrich estimated the distance that the particles below the arch moved between pulsations was 3% of a particle diameter, which is comparable to the 5% of a particle diameter dilation distance required for slip to occur in stick-slip simple shear experiments with granular materials [19]; however, further studies are required to determine if the proportionality constant (i.e. critical distance) in this regime is always a small fraction of the mean particle diameter.

Our experiments clearly revealed that at *large* average velocities of descent through the tube (10 – 60 mm/s), the pulsation frequency is independent of both discharge velocity and weak forcing due to silo structure oscillations. Hence it is reasonable to associate the observed pulsation frequency with the characteristic creep time. This finding also differs from experimental results obtained from studies of stick-slip motion in spring slider mechanisms where the period depends on the mechanical properties of the spring system (such as the spring constant and sliding mass) and is not solely controlled by the interaction between the sliding surfaces [18,21].

The lack of dependence of the pulsation frequency on discharge rate observed in this study is quite peculiar, as it implies that the distance the granular material falls during each pulsation increases as the discharge rate increases.

Wensrich [5] observed that the acceleration produced by each quaking impulse grew with distance traveled by the wave carrying the information of the impulse from the dynamic arch to the top of the silo. In contrast, the granular material accelerations recorded in these experiments with the accelerometer a fixed depth below the free surface did not change appreciably as the bed height decreased during discharge.

The granular material accelerations measured by Wensrich [5] were less than 15 m/s^2, while those measured in this study were typically more than 100 m/s^2. Tejchman [1] also observed silo wall acceleration levels greater than 100 m/s^2. Nonlinear effects that come into play at large amplitude disturbances or simply the fact that flow occurred in this system in a different frictional regime may be responsible for the height independence of the acceleration at the large accelerations seen in this study.

It is interesting to contrast the acceleration power spectra obtained with crushed glass and glass beads to see the effect of particle shape on granular dynamics. The power spectra for acceleration measurements in the glass beads (figure 13b) showed many harmonics of the pulsation frequency before the high frequency decay region was approached. The power spectra for crushed glass (figure 13a) showed only a few harmonics, followed by a band limited white noise region and then a high frequency decay. This suggests that the glass beads showed a highly correlated distributed response to slip which originated at the arch. Crushed glass had a significantly less correlated response, quite possibly because of the heterogeneity in particle shape and particle contacts between them. This is consistent with the suggestions by Mair et al. [25] that smooth round particles have force chains that are stable over a narrow range of orientations whereas, rough particles such as the crushed glass have force chains that are stable over a wider range of orientations. Consequently, the force chains in the glass beads break in a highly correlated manner during a pulsation, whereas those in the crushed glass break in a less correlated manner.

Surprisingly, all the power spectra for acceleration measurements inside the granular material for all tube and granular material combinations that pulsated decayed for frequencies above 1000 Hz. The high frequency cutoff of 1000 Hz was neither due to any limitation of the accelerometer (which could measure frequencies up to 10 KHz) or the lowest natural frequency of the tube (which was varied in these experiments and did not affect the high frequency cutoff). It may be related to the tube diameter, or to the particle size and particle density, which were not varied in the experiments.

The hypothesized difference in stress chain behavior between smooth and rough particles suggested by Mair et al. [25] may also explain the difference in the value of the critical height when an overload is imposed on the granular material. For rough particles the critical height decreased linearly with imposed overload, whereas for smooth particles, the critical height was independent of the imposed overload. Since the force chains in a granular material composed of smooth spheres will have narrow directionality, the effects of the imposed overload will be transmitted to the side walls of the silo rapidly, and will not affect stress levels between the silo wall and the granular material a significant distance away from the overload. These force chains form a bridge so that the bulk of the overload is transmitted to the silo walls. For rough particles, the force chains are less concentrated because friction and asperity interlocking allows rough particles to transmit forces in a variety of directions without failure. Because bridging in the granular material is less effective, the imposed overload is not screened and its effects on the stress field can be transmitted further in to the granular material. Consequently, the critical height decreases because stresses at the arch are large and allow pulsations to occur for a longer time during discharge, in agreement with studies that slip-stick friction is dependent on the local stress level [21].

Further work examining the shear and wall normal stresses in silos for different shapes and distributions of particle sizes with varying overloads would help in verifying these suggestions and in obtaining appropriate constitutive relations to describe granular material stress fields macroscopically, an area which is the subject of current debate [26].

Mair et al. [25] found that particle shape influences granular material sliding characteristics and influences stress transmission through the granular material. The present study confirms these findings, since granular materials made of the same glass with similar sizes but different shapes had different pulsation frequencies in the aluminum and galvanized steel tubes. This is because frictional characteristics depend on the roughness, hardness, shape, and chemical composition of the surface. In particular, since glass and aluminum have comparable hardness, particle shape will be the dominant factor determining the difference in sliding characteristics of crushed glass and glass beads. Since crushed glass has sharp edges, it can dig in to the aluminum surface more than the smooth glass beads, and so the adhesive stick time for crushed glass in the aluminum silo is longer than for glass beads in the same silo. Acrylic surfaces are prone to stick-slip motion [27]. As acrylic is softer than all the particles used in this study, the acrylic surface can be expected to be the dominant factor in determining the adhesive relaxation time for the stick-slip motion, and indeed it was found that the pulsation frequencies for all granular materials are similar in the acrylic silo. Glass beads had a lower slip frequency in the galvanized steel silo than crushed glass due to the different pressure interactions. Steel is harder than glass and since the steel surface is smooth, abrasive mechanical wear is negligible and surface chemical interactions are more significant. Since the glass beads used are smooth on a 10 μm length scales, they have a larger surface area in contact with the steel tube compared to the crushed glass. The glass beads therefore have greater adhesive forces, thus a larger adhesive relaxation time, and hence pulsate less often than the crushed glass particles in the steel tube. This is in agreement with observations that surfaces that are smooth on small length scales are more likely to undergo adhesive stick-slip friction since sticking and sliding can occur on the entire surface. Conversely, surfaces that are rough at the micron length scale are less likely to have stick-slip friction since the asperities can lock and prevent slip occurring at all contact points. These results are in accord with findings by Tejchman [1], Moriyama and Jimbo [2], and Jahagirdar [3] that to prevent stick-slip friction at the silo walls and hence silo quake, mass flow silos should have rough walls.

Tejchman and Niedostatkiewicz [17] and Kmita [7] had suggested that silo quake is due to a resonant interaction between the dynamics of the silo structure and the motion of the granular material. Hardow et al. [4] showed that a resonant interaction is not required for quaking to occur. This study confirms that the pulsation frequency need not be the same as the dominant natural frequency of the silo structure. Hardow et al. [4], whose study did not examine a variety of granular materials or change the frictional characteristics of the silo walls, suggested that wall friction was not the cause of silo quake, a finding which this study has shown is not always correct. Since their study was for a core flow silo, they did not consider the possibility that stick-slip friction can occur at sliding surfaces inside the granular material, as shown in the study by Nasuno et al. [18,] and not just between the granular material and the silo wall. The suggestion by Hardow et al. [4] that the silo is driven by the motion of the granular material is confirmed by the results of this study.

5 Summary

This study has shown that stick-slip motion generates silo music and silo quake. Silo music is driven by the stick-slip pulsating motion of the granular material during discharge and is associated with a resonance in the air column above the bed. When the pulsating motion disappears, so does the silo music. For small values of the spring constant, the pulsation frequency differs significantly from the dominant natural frequency of vertical oscillations of the silo. Hence, silo quake is not due to a resonant interaction between the granular material and the silo structure.

Over the range of discharge rates studied here (equivalent to average velocities of descent through the tube of 10 – 60 mm/s), the pulsation frequency was independent of discharge velocity and *weak* forcing due to silo structure oscillations. The pulsation frequency is controlled by the slow creep during the *stick* phase of the pulsating flow, with slip occurring on a much faster time scale. This slow creep is determined by the frictional interactions between the particles and the tube wall.

When the natural frequency of vertical oscillations of the silo is large, resonance can set in and the flow pulsates at the same frequency as the column. In this regime, the duration of the creep may be cut short by the oscillations of the silo.

Both silo music and flow pulsations stopped abruptly when the bed height fell below a critical value. It was found that the critical height could be changed by placing an overload in the case of crushed glass, but not smooth glass beads. This may be rationalized, although only speculatively at this point, on the basis of the differences in the behavior of stress chains in columns.

6 Acknowledgements

We are grateful to Professor A. Smits for many helpful discussions. The authors also wish to thank C. Wensrich for providing a copy of his thesis in advance of publication. BKM was supported by a Princeton University Francis Upton graduate fellowship. SFQ acknowledges financial support provided by the Derek Lidow senior thesis fund. This work was supported by the US Department of Energy CDE-FC26-00NT40971.

7 References

1. Tejchman J., "*Technical concept to prevent the silo honking*", Powder Technol. **106**, 7 (1999).
2. Moriyama R., Jimbo G., "*Reduction of pulsating wall pressure near the transition point in a bin*", Bulk Solids Handling **8,** 421 (1988).
3. Jahagirdar S., An Experimental Study of Sound Emission during Granular Flow. Department of Chemical Engineering, Indian Institute of Science, Bangalore, India (1999).
4. Hardow B., Schulze D., Schwedes J., "*An Experimental Analysis of the 'Silo Quaking' phenomenon*", Proc. Of the 3rd World Congress on Particle Technology, Brighton, England (1998).
5. Wensrich C.M., Analytical and Numerical Modeling of Quaking in Tall Silos, PhD Thesis, University of Newcastle, Australia (2002).

6. Phillips C.E.S., "*Electrical and other properties of sand"*, Not. Proc. Roy. **19,** 742 (1910).
7. Kmita J., "*Silo as a system of self-induced vibration*", ASCE J. of Struct. Eng. **111,** 190 (1985).
8. Tejchman J., Gudehus G.,*"Silo-music and silo-quake, experiments and a numerical cosserat approach",* Powder Technol. **76**, 201 (1993).
9. Fung Y.C., Sechler E.E., Kaplan A., "*On the vibration of thin cylindrical shells under internal pressure*", J. of the Aeronautical Sciences, **24(9)**, 650 (1957).
10. Muite B.K.,The effects of boundaries on granular and fluid mechanics, M.S.E. Thesis, Princeton University, Princeton, New Jersey, USA (2003).
11. Quinn S.F., Silo Music, B.S. Thesis, Princeton University, Princeton, New Jersey, USA (2002).
12. Rayleigh J.W.S., The Theory of Sound vol. II, Dover Publications (1945).
13. Bergé P., Pomeau Y., Vidal C., Order within Chaos, Wiley (1984).
14. Nedderman R.M., Statics and Kinematics of Granular Materials, Cambridge University Press (1992).
15. Baxter G.W., Behringer R.P., Fagert T., Johnson G.A., "*Pattern Formation in Flowing Sand*", Phys. Rev. Lett., **62(24)**, 2825 (1989) .
16. Perry M.G., Handley M.F., "*The Dynamic arch in free flowing granular material discharging from a model hopper*", Trans. Instn. Chem. Engrs. **45**, T367 (1967).
17. Tejchman J., Niedostatkiewicz M., "*Resonance effects during granular flows in silos*", Proc. International Congress for Particle Technology, Nuremburg, Germany (2001).
18. Nasuno S., Kudrolli A., Bak A., Gollub J.P., "*Time-resolved studies of stick-slip friction in sheared granular layers*", Phys. Rev. E **58**(2), 2161 (1998).
19. Géminard J.C., Losert W., Gollub J.P., "*Frictional mechanics of wet granular material*", Phys. Rev. E **59**(5), 5881 (1999).
20. McCabe R.P., "*Flow patterns in granular materials in silos*", Geotechnique **24**, 45 (1974).
21. Bowden F.P., Tabor D., The friction and lubrication of solids, Oxford University Press (1950).
22. Krim J., *"Friction at macroscopic and microscopic length scales"*, Am. J. Phys. **70(9)**, 890 (2002).
23. Berman A.D., Ducker W.A., Israelachivili J.N., "*Experimental and theoretical investigation of stick-slip friction mechanisms*" in Persson B.N.J., Tosatti E.,ed. Physics of Sliding Friction, Kulwer Academic Publishers (1996).
24. Cates M.E., Wittmer J.P., Bouchaud J.P., Claudin P., "*Jamming, force chains, and fragile matter"*, Phys. Rev. Lett. **81**(9), 1841 (1998).
25. Mair K., Frye K.M., Marone C., "*Influence of grain characteristics on the friction of granular shear zones*", J. of Geo. Res. **107(B10),** 2219 (2002).
26. Vanel L., Claudin Ph., Bouchaud J.-Ph., Cates M.E., Clément E., Wittmer J.P., "*Stresses in Silos: Comparison between theoretical models and New Experiments"*, Phys. Rev. Lett. **84(7)**, 1439 (2000).
27. Bouissou S., Petit J.P., Barquins M., "*Normal load, slip rate and roughness influence on the polymethylmethacrylate dynamics of sliding 1. Stable sliding to stick-slip transition*", Wear **214**, 156 (1998).

Table 1
Tube properties

Tube Material	Length (m)	ID (mm)	Wall Thickness (mm)	Surface Finish	Experimental Natural Frequency (Hz)
6061-T6 Aluminum Alloy	1.8	63.7±0.1	5.1±0.1	Smooth	3000 ±100 (Small peak at 1500)
Untreated Steel	1.8	63.8±0.1	5.7±0.1	Rough	2900 ±100 (Small peak at 1400)
Galvanized Steel	1.8	63.2±0.1	5.2±0.1	Smooth	2800 ±100 (Small peak at 1400)
Cast Acrylic	1.5	63.5±0.1	6.4±0.1	Smooth	350 ±100

Table 2: Granular Material Properties

Material	Supplier	Particle Size (μm)	Particle Density (g/cm^3)	Angle of Repose (°)
Crushed Glass	Potters Industries	450±50	2.5±0.1	28±1
Ballotini Impact Beads	Potters Industries	480 ±60	2.5±0.1	26±1
Washed and Ignited Standard Ottawa Sand	EMD Science	400±100	2.7±0.1	33±1

Table 3

Variation of critical height with silo wall and granular material properties

Silo wall material	Granular material	Critical height[a] (m)
Aluminum	Crushed glass	0.9
Aluminum	Glass beads	1.3
Acrylic	Crushed glass	0.8
Acrylic	Glass beads	0.6
Acrylic	Sand	0.7
Galvanized Steel	Crushed glass	1.3
Galvanized Steel	Glass beads	1.4
Galvanized Steel	Sand	1.4

Note: [a] The accuracy of the critical height data is ± 0.1 m.

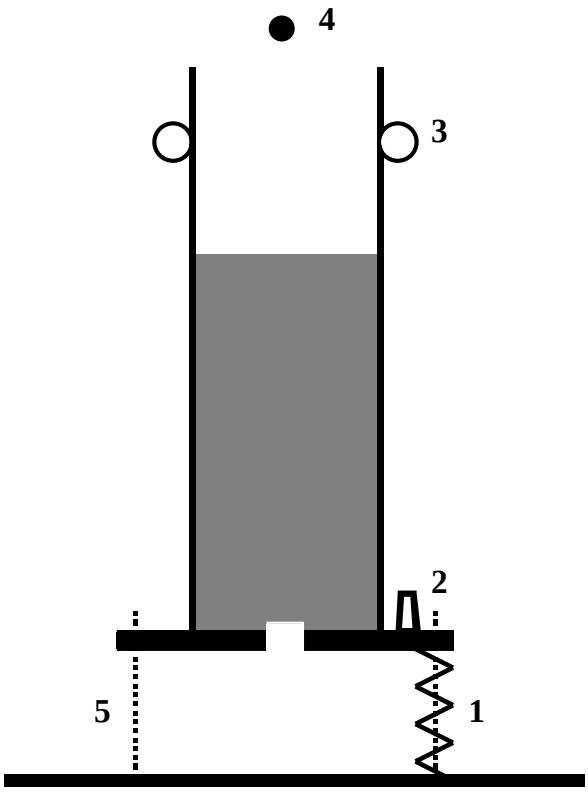

Fig. 1: Experimental setup for vertical acceleration and sound measurements. The numbers indicate (1) spring on positioning slider, (2) accelerometer, (3) positioning roller, (4) microphone, (5) positioning slider.

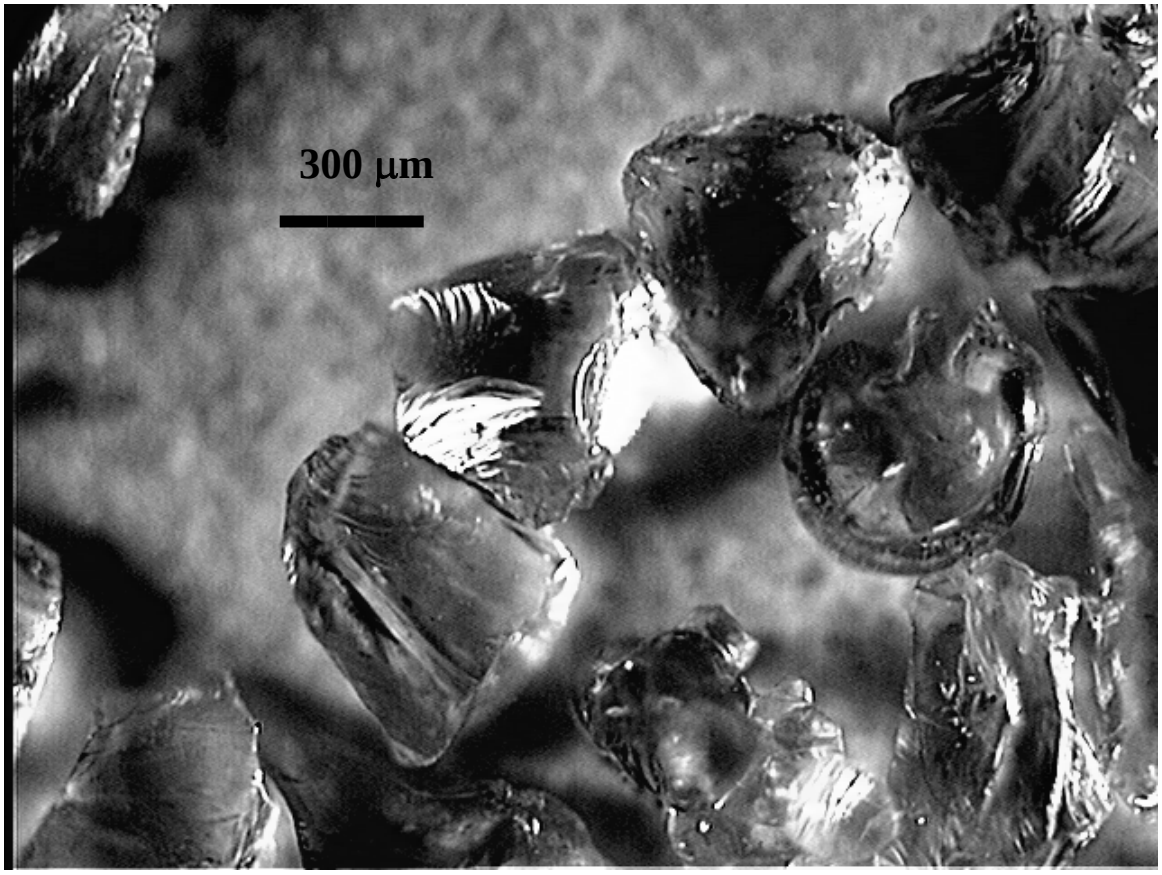

Fig. 2: A photograph of the crushed glass.

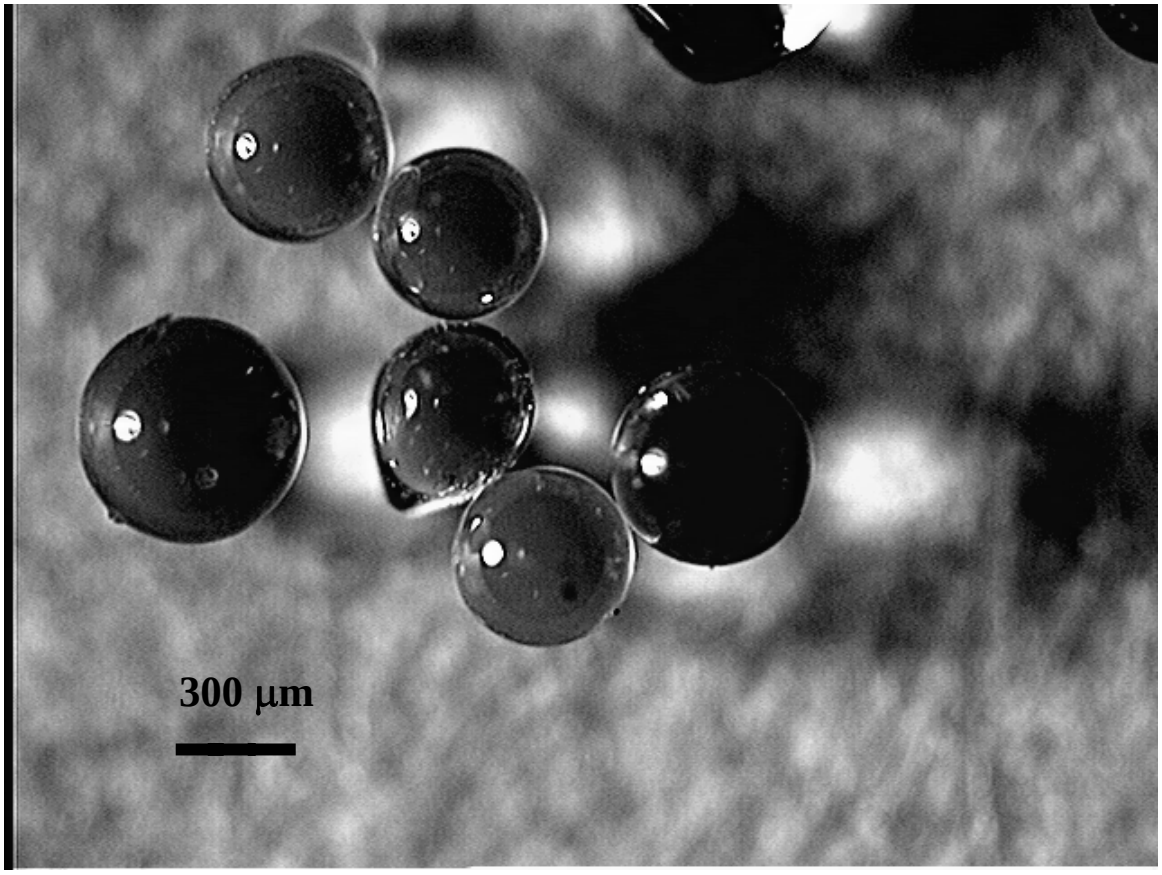

Fig. 3: A photograph of the glass beads.

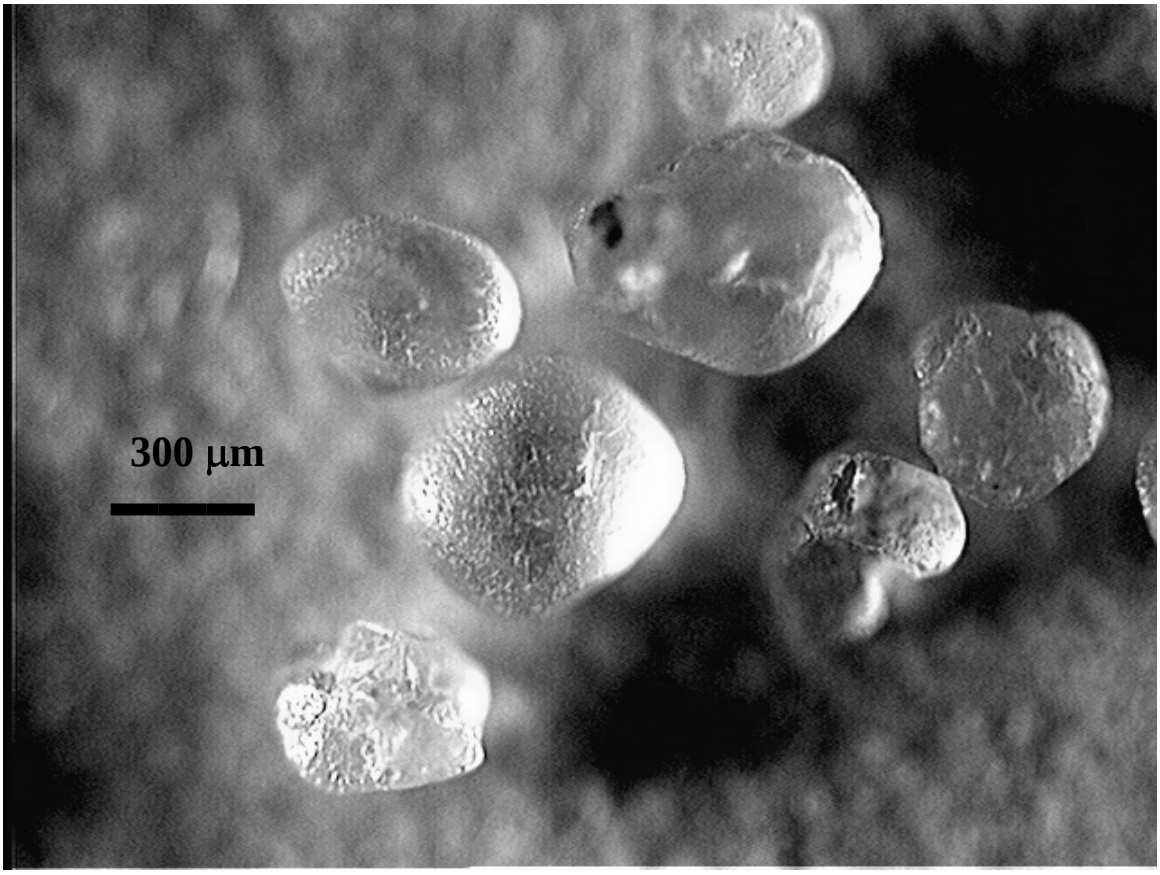

Fig. 4: A photograph of the sand particles.

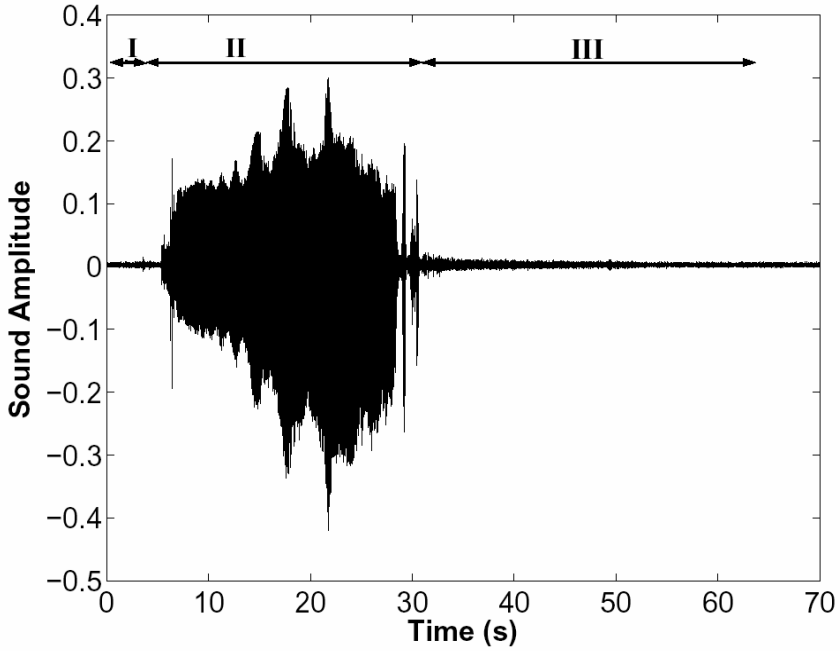

Fig. 5: Variation of sound level with time during discharge of sand from an acrylic tube of 76 mm outer diameter, wall thickness 3 mm, and having an orifice of diameter 19 mm. Indicated on the figure are; region I – no flow, region II – flow with pulsations and region III – flow after pulsations have ended.

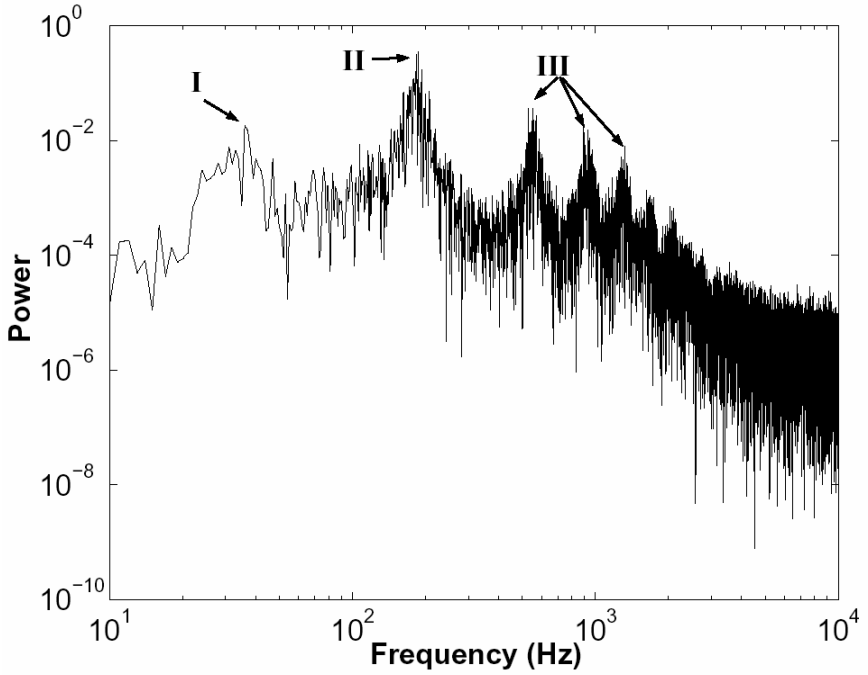

Fig. 6: Typical power spectrum for sound measurements during silo music when sand is discharged from an acrylic tube of 76 mm outer diameter, wall thickness 3 mm, and having an orifice of diameter 19 mm. Indicated on the figure are the pulsation frequency (I), the dominant sound frequency (II) and the higher harmonics of the dominant sound frequency (III).

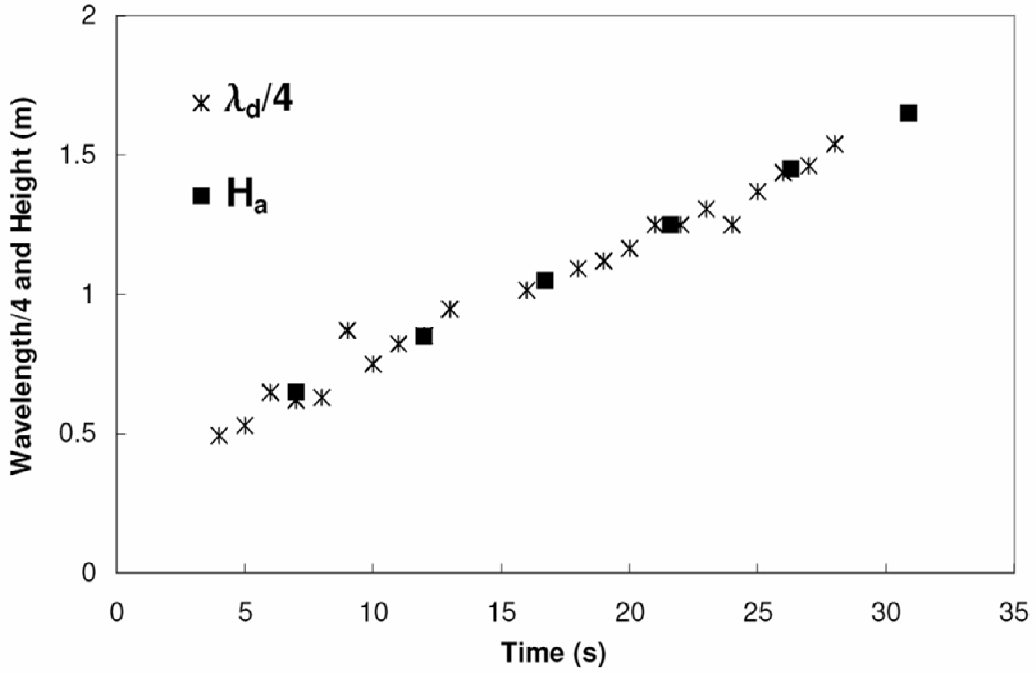

Fig. 7: Variation of the dominant quarter wavelength ($\lambda_d/4$) and the height of the air column (H_a) with time during discharge of sand from an acrylic tube of 76 mm outer diameter, wall thickness 3 mm, and having an orifice of diameter 19 mm.

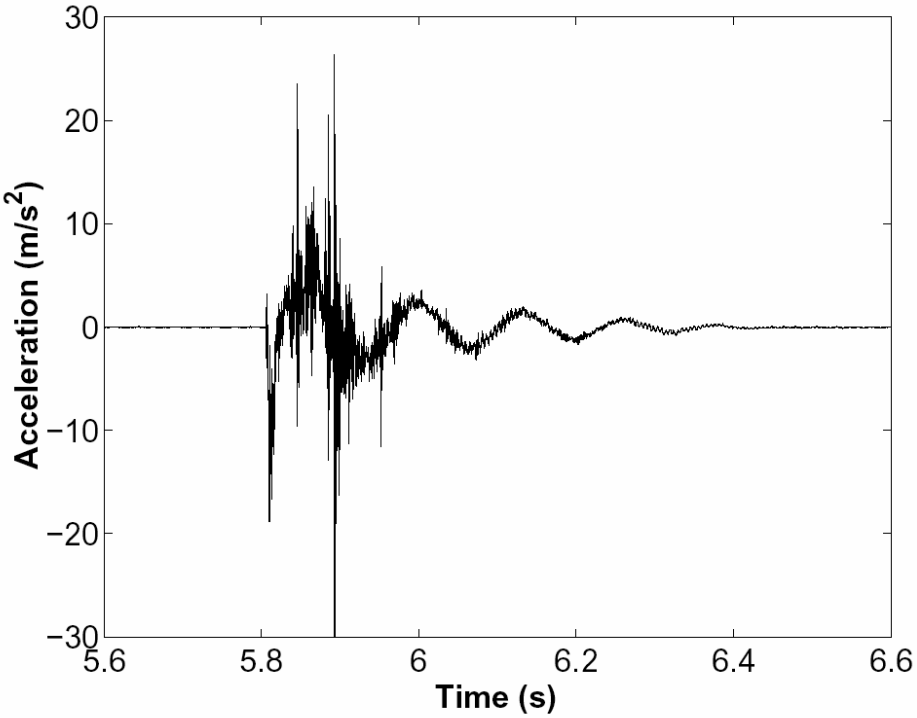

Fig. 8: Typical acceleration measurement for free oscillations of the filled aluminum silo on a 31 N/mm spring after it has been struck.

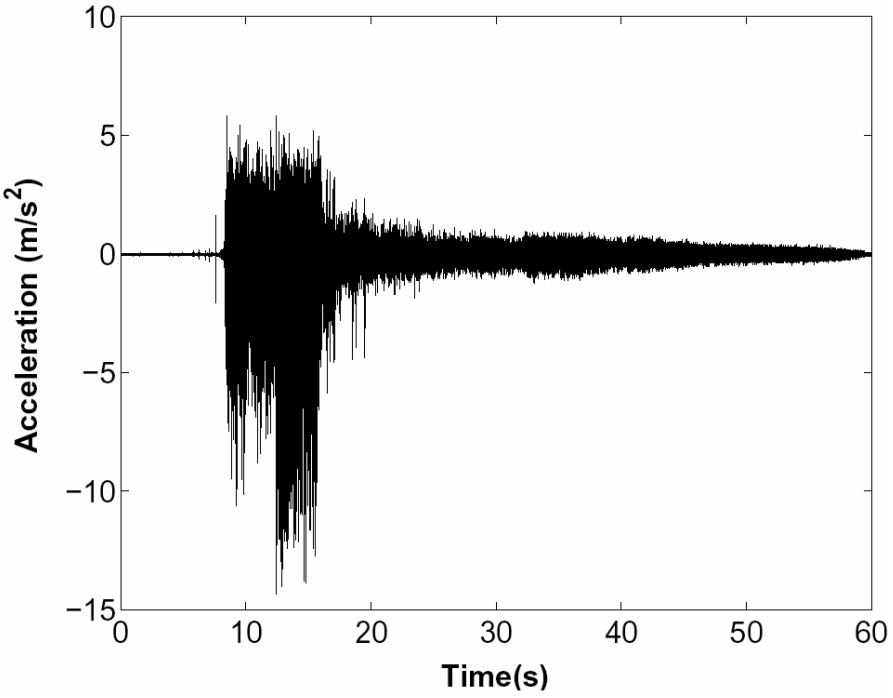

Fig. 9: Vertical acceleration measurements on the base of the aluminum silo during discharge of crushed glass through a 1.9 cm orifice. The silo was mounted on a 31 N/mm spring. Indicated on the figure are; region I – no flow, region II – flow with pulsations and region III – flow after pulsations have ended.

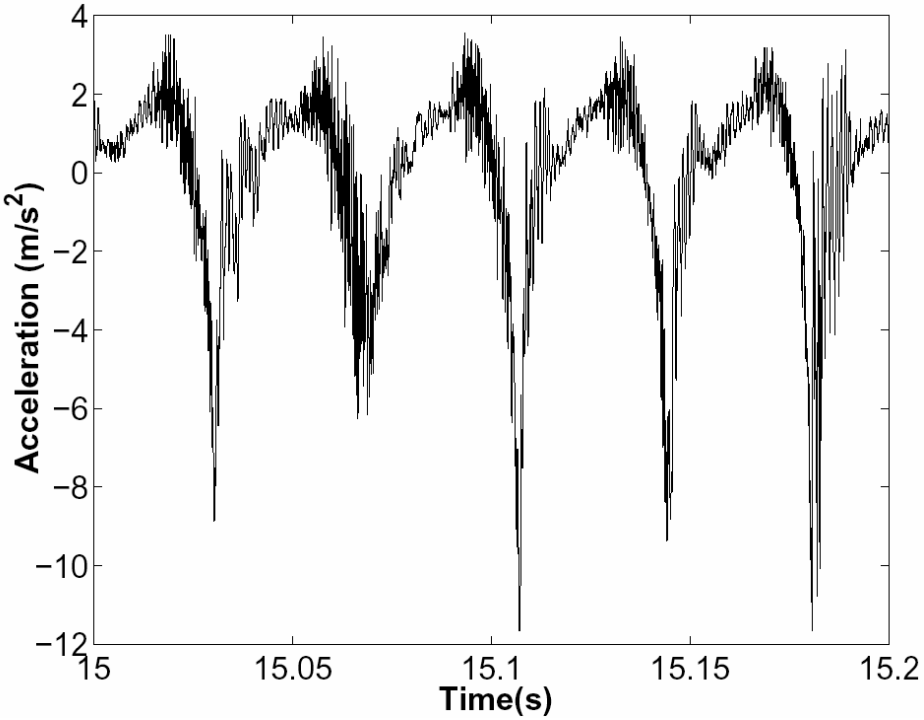

Fig. 10: Close-up showing individual pulsations measured by the accelerometer on the silo structure for the flow in Fig. 9.

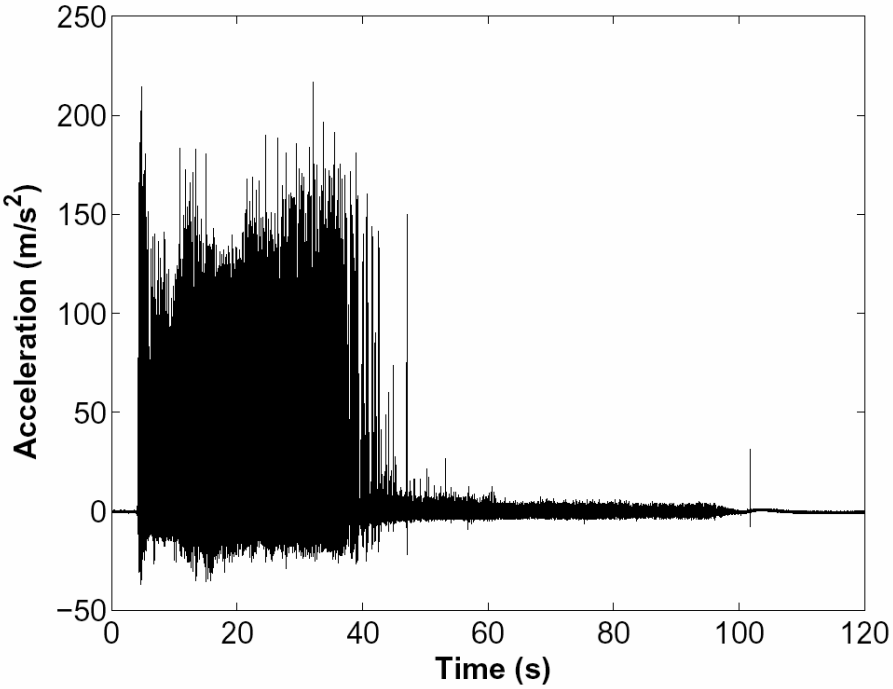

Fig. 11a: Vertical acceleration measurements when the accelerometer was embedded in the crushed glass. The aluminum silo had a 1.3 cm orifice and was mounted on a 31 N/mm spring. Indicated on the figure are; region I – no flow, region II – flow with pulsations and region III – flow after pulsations have ended.

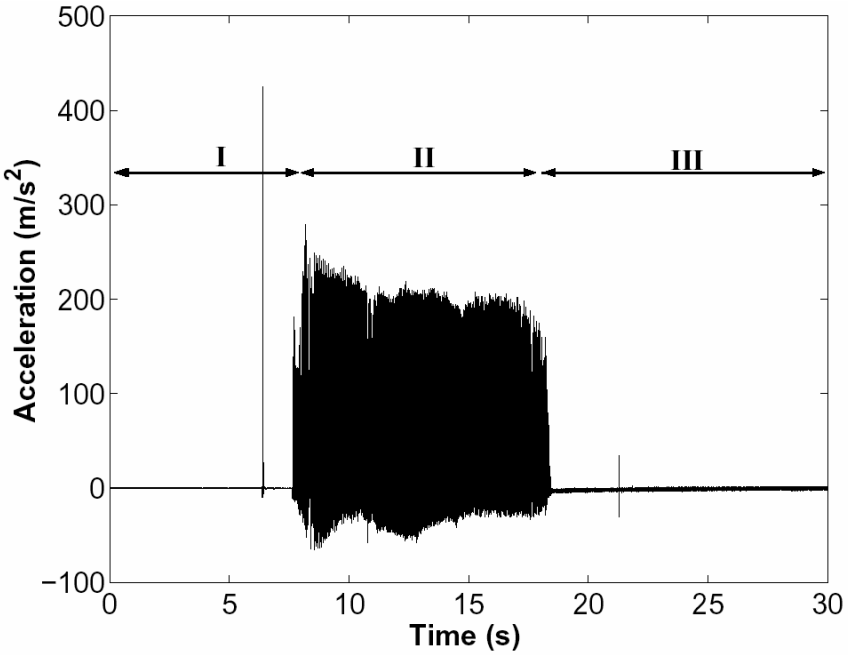

Fig. 11b: Vertical acceleration measurements when the accelerometer was embedded in the glass beads. The aluminum silo had a 1.9 cm orifice and was mounted on a 22 N/mm spring. Indicated on the figure are; region I – no flow, region II – flow with pulsations and region III – flow after pulsations have ended.

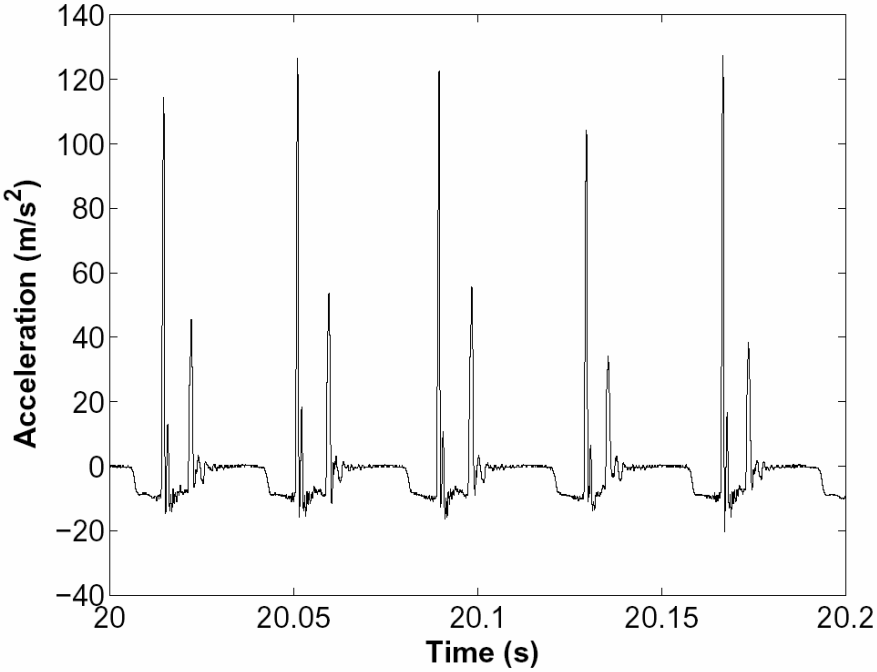

Fig. 12a: Close-up showing individual pulsations measured by the accelerometer in the granular material for the flow in Fig. 11a.

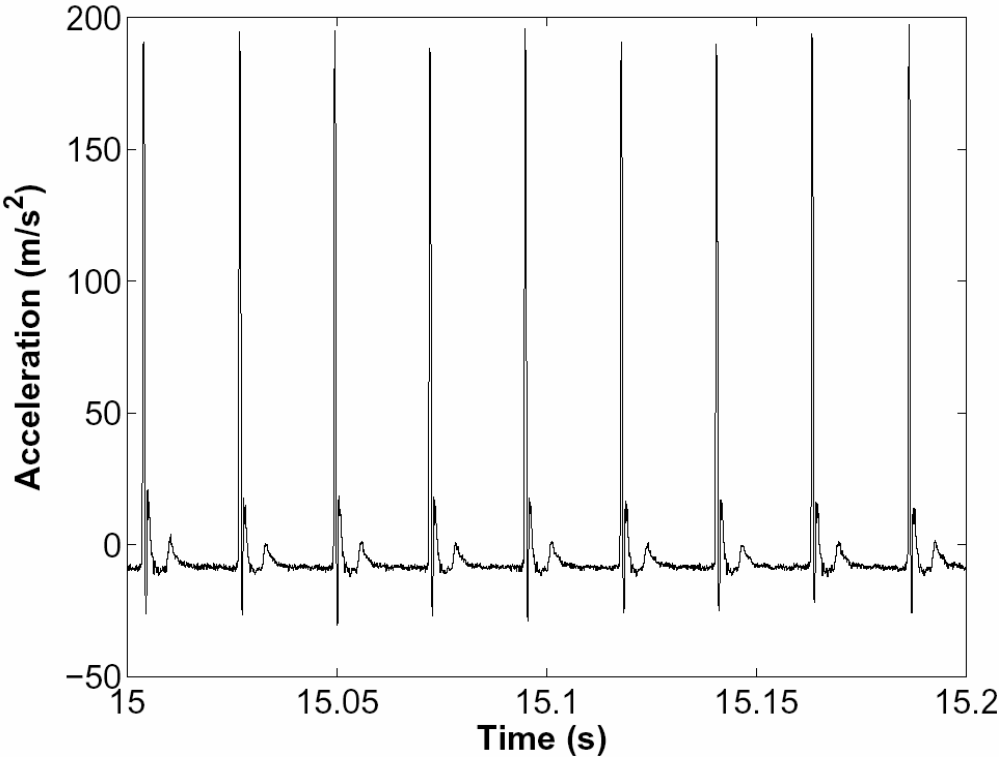

Fig. 12b: Close-up showing individual pulsations measured by the accelerometer in the granular material for the flow in Fig. 11b.

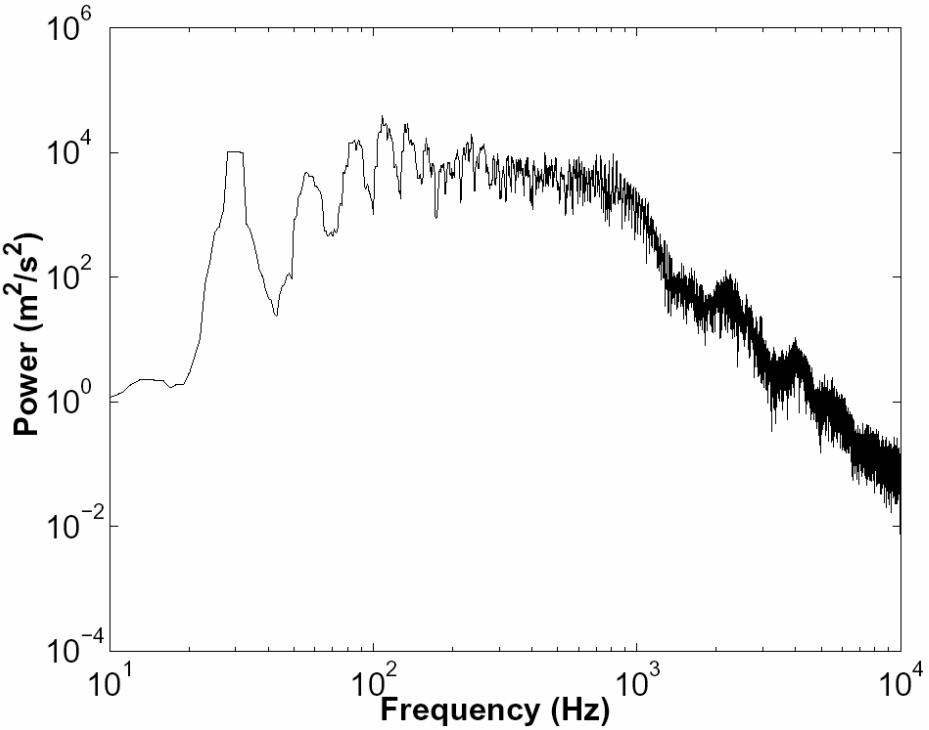

Fig. 13a: Power spectrum for the 20th second of the measurements in Fig. 11a. The power spectrum has been averaged over 4 points in frequency to make average trends clearer.

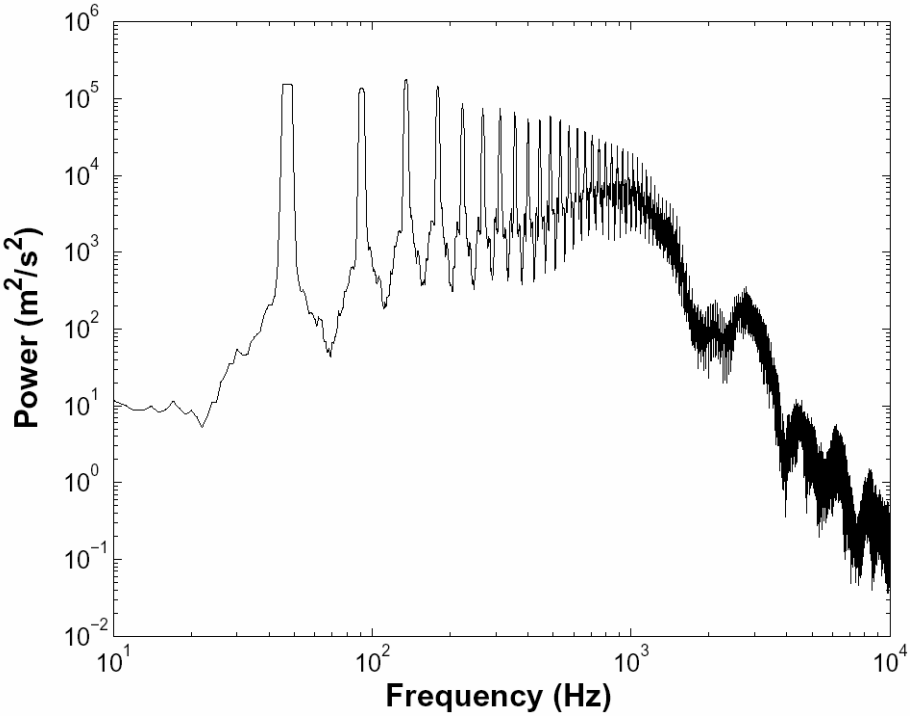

Fig. 13b: Power spectrum for the 15th second of the measurements in Fig. 11b. The power spectrum has been averaged over 4 points in frequency to make average trends clearer.

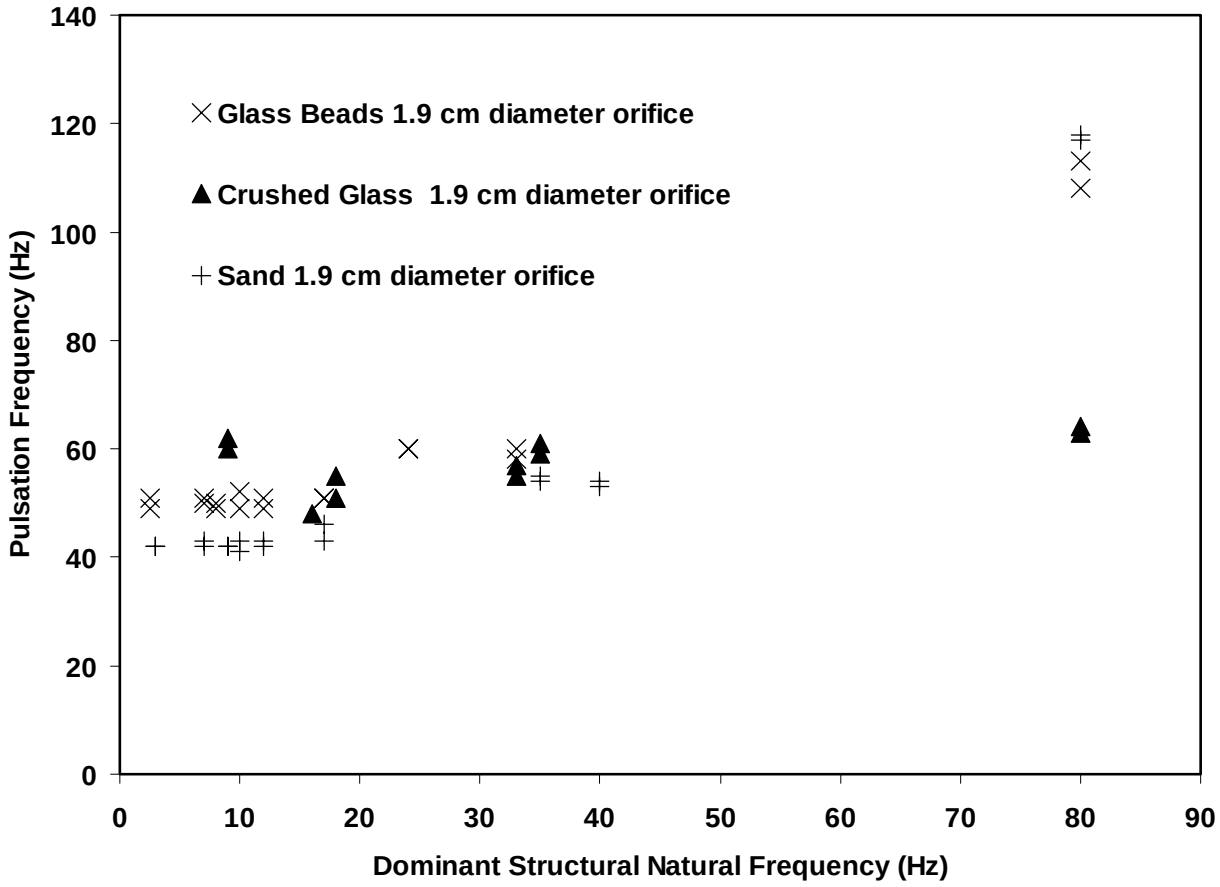

Fig. 14: Dominant structural natural frequency against pulsation frequency for granular materials discharging from the acrylic tube.

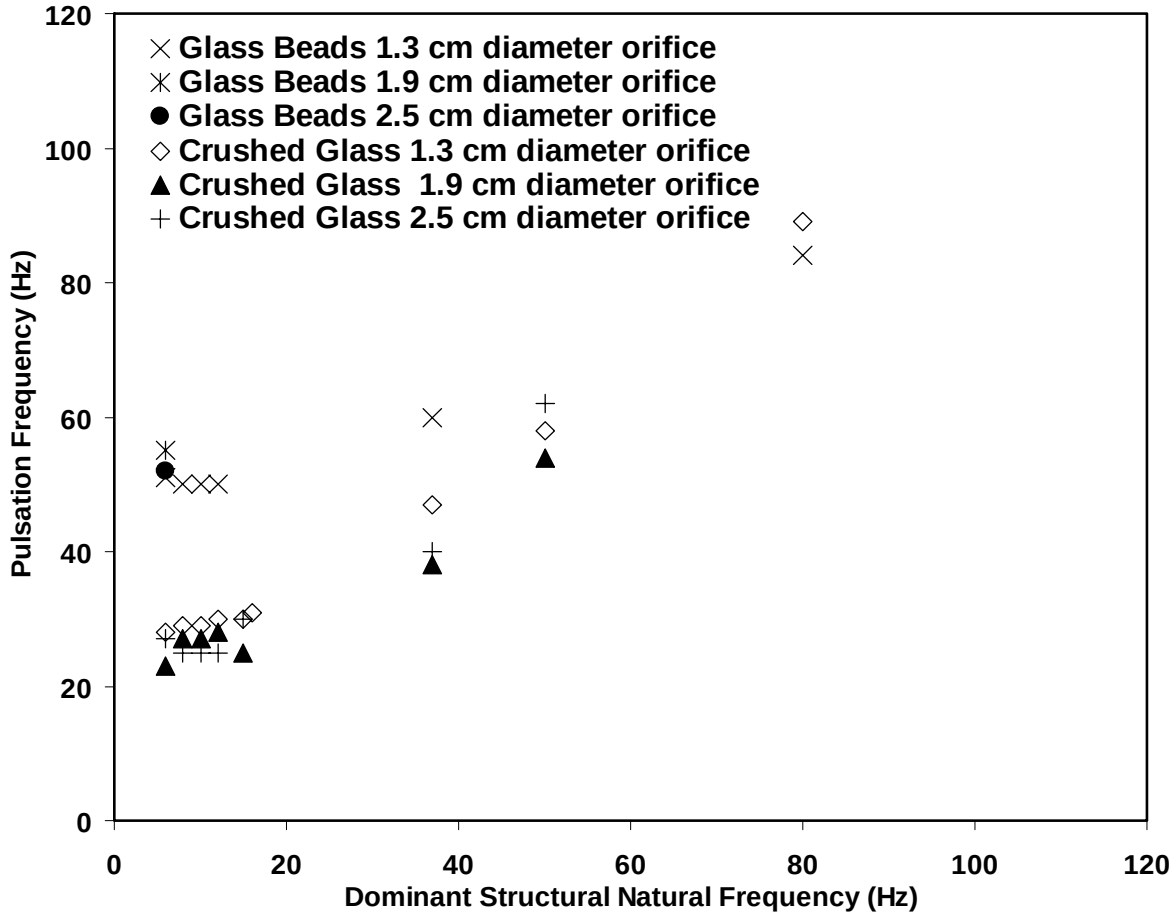

Fig. 15: Dominant structural natural frequency against pulsation frequency for granular materials discharging from the aluminum tube.

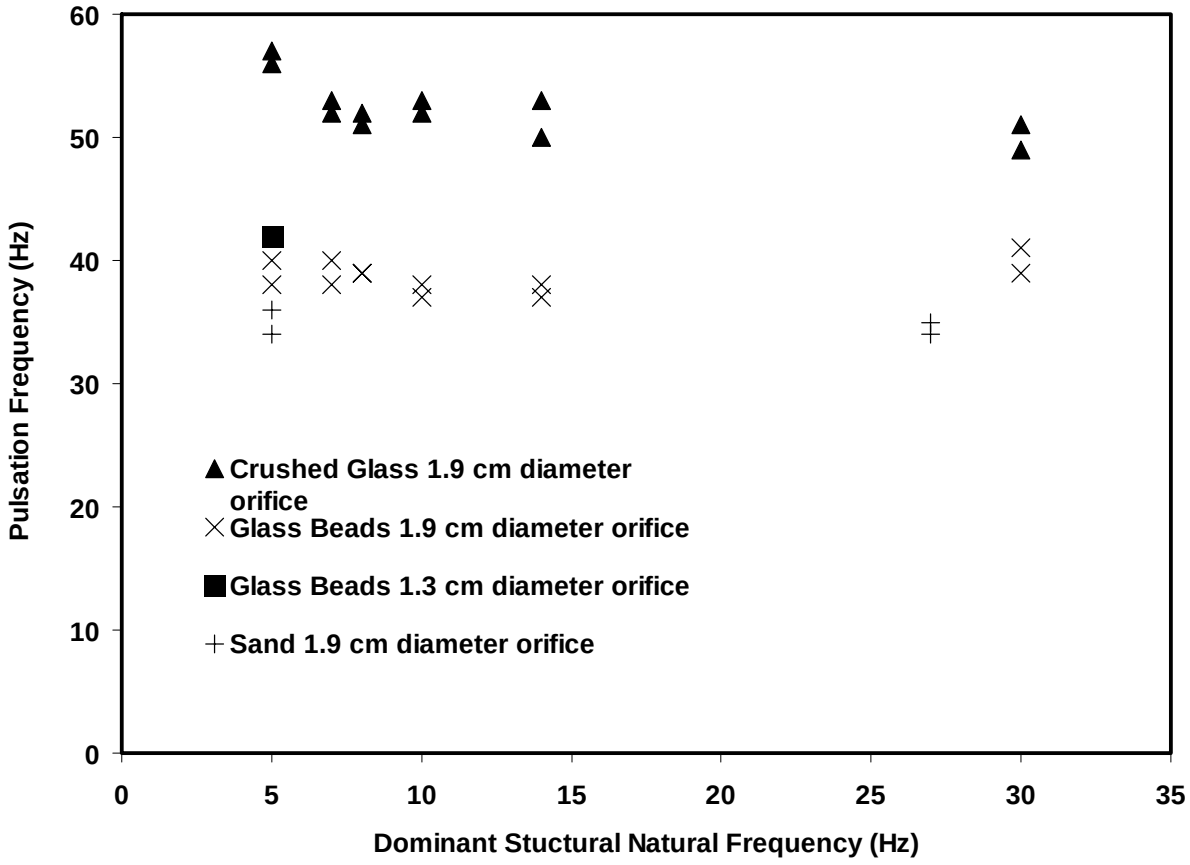

Fig. 16: Dominant structural natural frequency against pulsation frequency for granular materials discharging from the galvanized steel tube.

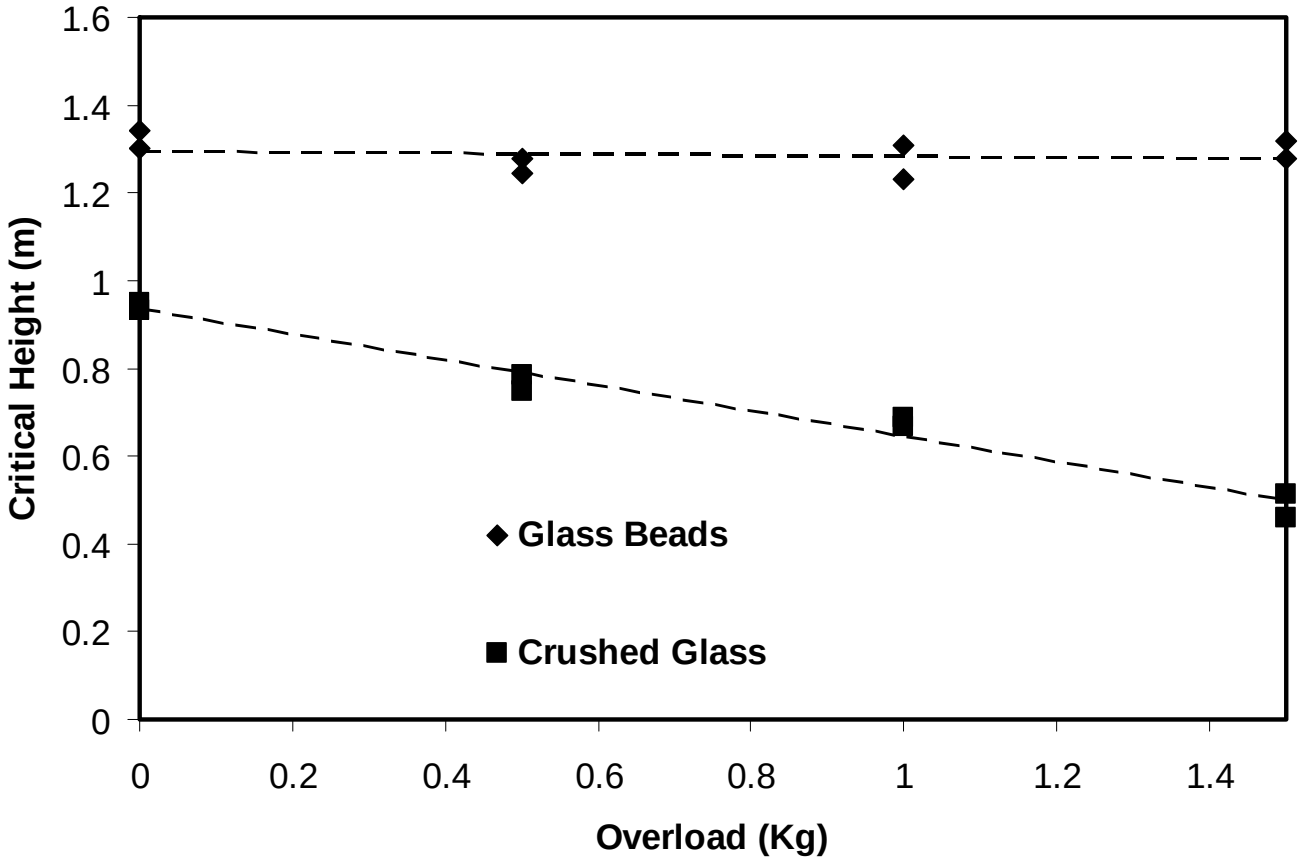

Fig. 17: Variation of critical height with overload for glass beads and crushed glass in the aluminum tube.